NGL-24-005-008

COSMIC RAY GROUP

School of Physics and Astronomy

UNIVERSITY OF MINNESOTA

A BALLOON BORNE X-RAY SURVEY

OF THE CYGNUS REGION*

by

Charles Peter Reinert

Technical Report
CR-132

June, 1969

School of Physics and Astronomy
University of Minnesota
Minneapolis, Minnesota

*A thesis submitted to the faculty of the Graduate School of the University of Minnesota in partial fulfillment for the requirement for the Degree of Doctor of Philosophy.

A BALLOON BORNE X-RAY SURVEY

OF THE CYGNUS REGION

A THESIS

SUBMITTED TO THE FACULTY OF THE GRADUATE SCHOOL

OF THE UNIVERSITY OF MINNESOTA

BY

CHARLES PETER REINERT

IN PARTIAL FULFILLMENT OF THE REQUIREMENTS FOR THE DEGREE OF

DOCTOR OF PHILOSOPHY

JUNE, 1969

TABLE OF CONTENTS

	Page
List of Figures	iii
I. INTRODUCTION	1
II. DESCRIPTION OF THE EXPERIMENT	2
A. The X-ray detector.	2
B. Electronics and orientation system.	5
III. THEORETICAL BASIS OF THE DETECTOR	6
A. Fundamental interactions of photons (10-500 Kev) with matter.	6
B. The response of NaI(Tℓ) to photons of 10 to 500 Kev.	10
C. The conversion of visible light into a usable electronic signal.	12
IV. SUMMARY OF FLIGHT	13
A. Preflight calibration.	13
B. The flight.	14
V. ANALYSIS OF THE DATA	15
A. Expected response of the detector on the celestial sphere.	15
B. Separation of sources from the background.	16
C. Corrections for instrumental dead times, and for atmospheric and gondola absorptions.	23
VI. DISCUSSION OF RESULTS	27
A. The spectrum of Cyg X-1/X-3.	27
B. On the variability of Cyg X-1.	28
C. The spectra of Cygnus X-2/X-4 and X-3.	29
D. The diffuse X-ray background.	31

	Page
VII. MODELS FOR X-RAY GENERATION BY LOCALIZED SOURCES	34
A. Synchrotron radiation.	35
B. Inverse Compton radiation.	37
C. Thermal bremsstrahlung.	39
D. Black body radiation.	40
VIII. COMPARISON OF DATA WITH THEORETICAL MODELS	40
A. Cygnus X-1.	40
B. Cygnus X-2/X-4 and X-3.	44
D. Agreement of the diffuse X-ray background.	45
APPENDIX A - DISCUSSION OF ERRORS	48
A. Error in instrument azimuth.	48
B. Error in zenith angle.	48
C. Uncertainty in absorption factors.	47
D. Uncertainty in background.	48
APPENDIX B - DERIVATION OF RESPONSE FUNCTION EFF (t)	50
APPENDIX C - DERIVATION OF THE CORRECTION FOR DEAD TIME IN THE FLIGHT ELECTRONICS	54
TABLES	56
BIBLIOGRAPHY	59
ACKNOWLEDGMENTS	62

FIGURES

Figure 1. Outline of the X-ray detector. FWHM of the detector with this shield configuration is ~22 degrees.

Figure 2. Relative light collection efficiency in the liquid scintillator chamber, as a function of distance vertically above the phototube face, for several angles around the periphery of the chamber using only one phototube. Also shown is the response expected for three such tubes, spaced symmetrically around the periphery of the chamber.

Figure 3. Block diagram of the flight electronics.

Figure 4. The X-ray attenuation and absorption coefficients for various processes in NaI(Tℓ). From Evans, R., <u>The Atomic Nucleus</u> (McGraw-Hill, 1955).

Figure 5. The X-ray spectrum of Cd^{109} (22, 88 Kev) as seen by the flight crystal and photomultiplier system. Pulse height analysis by a 200 channel multichannel analyzer.

Figure 6. The X-ray spectrum of Cd^{109} as viewed by the flight electronics using the flight crystal and photomultiplier tube. The peak in channels 2 and 3 corresponds to 22 Kev, that centered in channel 8 to 88 Kev. Channel width is approximately 11.7 Kev.

Figure 7. The angular response of the detector-shield configuration at 22, 88 and 130 Kev.

Figure 8. Averaged counting rates for two energy channels for the period of observation of the four sources. Shown at the bottom of the figure are the Eff(t) curves for the four sources.

Figure 9. A map of the Cygnus region showing the locations of the four sources; superimposed is the FWHM of the angular response of the experiment. The dotted circle represents the locus of the central axis of the telescope due to rotation by the line twister. As time increases, the detector moves across the map from left to right.

Figure 10. A scattergram of detector counting rate R(t) versus the efficiency Eff(t) of the detector. The vertical error bars constitute a standard deviation for the approximately 100 events represented by each data point.

Figure 11. Convergence of the weighted least squares fit as a function of the number of iterations. The rate of convergence was not significantly affected by the signal to noise ratio of the particular channel. The "AX + B" fits and "AX + known background" fits converged at comparable rates.

Figure 12. Background counting rates for several energy channels. The dotted lines bridging the interval where no background rates are available represent the "interpolated" background value used to compute the flux from Cygnus X-1; the single data points near the middle of the interval represent the background calculated via a weighted least squares fit. Transit for Cygnus X-1 occurred at 1112 hours UT, near the center of the interval.

Figure 13. The spectrum of Cygnus X-1 as measured at the detector.

Figure 14. The angular distribution for photons scattered off electrons by the Compton process. Curves shown are for $\alpha=.1$, and $\alpha=.4$, where $\alpha=h\nu_0/m_eC^2$, thus for 50 and 200 Kev. The radial distance is proportional to the probability per unit solid angle that the photon will scatter at a given angle θ.

Figure 15. The photon spectrum of Cygnus X-1 extrapolated to the top of the atmosphere, as measured by this experiment. The horizontal error bars represent the width of the energy channel; vertical error bars are principally due to the uncertainty in the background rate and are conservatively equivalent to a standard deviation.

Figure 16. The photon spectrum of Cygnus X-1, extrapolated to the top of the atmosphere, as measured by this experiment and by other workers.

Figure 17a. The energy spectrum of Cygnus X-1 extrapolated to the top of the atmosphere, as measured by this experiment.

Figure 17b. The energy spectrum of Cygnus X-1 extrapolated to the top of the atmosphere, as measured by this experiment and by other workers.

Figure 18. Fluxes measured for Cygnus by various workers, in several energy intervals.

Figure 19. The spectrum of Cygnus X-2/X-4 extrapolated to the top of the atmosphere as measured by this experiment and by other workers.

Figure 20. The spectrum of Cygnus X-2/X-4 shown over an extended energy range to include flux from the optical counterpart of X-2. Two possible exponential fits are shown.

Figure 21. The flux of Cygnus X-1/X-3 as measured at the detector as a function of time, assuming that all flux comes from X-1. Error bars shown represent the uncertainty due to the background rate.

Figure 22. The spectrum of Cygnus X-3, extrapolated to the top of the atmosphere as measured by this detector and by other workers.

Figure 23. The counting rate for a representative low energy channel as a function of pressure during the ascent of the balloon. The counting rate above 10 mb is assumed to be principally due to the atmospheric background, and the line fitted to the data between 10 and 40 mb is used to extrapolate the "atmospheric" counting rate to lower pressures, after the technique of Bleeker et al.[20] The extra-terrestrial contribution is represented by the arrows.

Figure 24. The photon spectrum of the diffuse extra-terrestrial X-ray flux, as measured by this experiment and by other workers.

Figure 25. The energy spectrum of Cygnus X-1 shown over an extended range of energies.

Figure 26. The photon spectrum of the diffuse extra-terrestrial X-ray flux shown over an extended range of energies.

Figure 27. Vector diagram for calculation of the angle between two celestial directions given the azimuth and altitude of each vector.

I. INTRODUCTION

Localized celestial sources of X-rays were first discovered by Giacconi et al[1] during a rocket flight in 1963 to search for X-rays from the moon, and confirmation was obtained on later flights. Clark[2] in 1964 observed significant increases in his balloon borne X-ray detector whenever the Crab Nebula was in the field of view of the detector. In the past 7 years, more than 20 sources have been cataloged. Most of the sources discovered thus far are more readily observable by rocket flights (low energies, 1 - 10 Kev and altitudes $\sim$100 Km) than by balloon borne instruments (>20 Kev, 25 Km altitude) since the source spectra are fairly steep, and the fluxes are low enough so that "background" fluxes from cosmic ray produced secondaries rapidly become greater than those from the celestial sources as one descends to thicker atmospheric depths. Further difficulty in the observation of celestial X-rays by a balloon borne detector is caused by Compton and photoelectric absorption processes as the photons pass through the residual atmosphere. The principal advantage of balloon borne detectors is their greater time aloft (several hours) compared to the few minutes of observation time afforded by rocket flights, and this has made possible statistically significant measurements of the fluxes of the celestial sources out to 100 Kev and beyond, despite the lower fluxes at the higher energies. Flux measurements over as broad an energy range as possible are highly desirable from an astrophysical point of view, since few of these sources have been optically identified, and the energy generation mechanisms remain questions of considerable interest.

Sources in the constellation Cygnus have been observed by several investigators.[3,4,5,6,7] The positions of the four known sources in this region are believed to have been given most accurately by Giacconi[3] and workers and are listed in Table 1 together with the fluxes measured at low energies. Cygnus X-1 has been observed as the strongest of the four in the range 1-10 Kev and also at balloon energies (>20 Kev) although balloon borne detectors usually have difficulty resolving X-1 from X-3 because of their proximity on the celestial sphere. Only one group[12] has reported of measuring fluxes from X-1 beyond 100 Kev, and their data imply a steepening of the spectrum beyond approximately 100 Kev. The data from the experiment described in the present work serve to substantially confirm these high energy results, and to shed further light on the nature of the energy generation mechanism for Cygnus X-1.

II. DESCRIPTION OF THE EXPERIMENT

A. The X-ray detector. The essential features of the X-ray detection system are shown in Figure 1. The central detector is composed of a 100 cm^2 area by 3 cm. thick NaI(Tl) crystal optically coupled to a 5" EMI type 9530 photomultiplier tube. It is mounted down inside a cylindrical well of graded shielding material, consisting of appropriate thicknesses of Pb, Sn and Cu, plus 6 cm. of Nuclear Enterprises Type NE211 liquid scintillator used as an anticoincidence element. The full width at half maximum (FWHM) response of the central detector in this shield configuration is approximately 22 degrees.

One of the fundamental observational problems of balloon borne X-ray astronomy is the inevitable presence of a background composed of cosmic ray produced secondary X-rays, and electrons and other charged particles. Even when constant in time, this background imposes an effective lower limit to the flux which can be observed by a balloon borne instrument in a flight time of a few hours, and when time varying, can make flux measurements from an extra-terrestrial source rather uncertain. This flux is almost isotropic as viewed by the instrument, and the best that one can do is to try to minimize the detection of this background via suitable shielding. A second background source is due to interaction of cosmic rays with the shielding material of the instrument itself. For this reason merely passive shielding (e.g. Pb) is not as effective as an "active" shield (e.g. NaI(Tl)). However, inorganic crystal scintillators such as NaI(Tl) become very expensive and very susceptible to thermal and mechanical shock in geometries suitable for shielding a 100 cm^2 detector area. Shielding against the background was therefore done semi-actively via passive shields of Pb, Sn and Cu, in conjunction with the liquid scintillator, as shown in Figure 1. The Pb on the outside is effectively opaque (<10% transmission) to X-rays of energy $E < 230$ Kev. However, bombardment by cosmic rays and high energy X-rays will cause the "characteristic" X-ray spectrum of Pb to be emitted, with X-ray emission near 88 Kev. Since the Pb is somewhat transparent to its characteristic emission, an eighth inch layer of Sn is used beneath the Pb. Since the atomic numbers of Pb and Sn are different, the X-ray emission lines are at different energies, and we find the characteristic emission of Sn at 29.2 Kev and lower energies. Thus Sn acts as a rather good absorber of the X-ray emission spectrum of Pb, but in turn has its own emission spectrum, at lower energies. We then further line the barrel of the telescope with .040" of Cu, which has emission lines at 8.27 Kev and lower energies (below our range of analysis) and absorbs the emission spectrum of the Sn. The liquid scintillator NE211 chiefly gives protection against charged particles, since the average atomic number of its constituents (chiefly toluene) is of the order of ~7, and interactions by X-rays are therefore mostly due to the Compton process. The ~6 cm. thickness of NE211 can detect 90% of X-rays of energy 28 Kev and below, but only 60% at 80 Kev. On the other hand, the liquid scintillator should be essentially 100% effective in charged particle detection, limited principally by the efficiency of light collection. Figure 2 shows the collection efficiency for light from a photodiode as a function of the distance vertically above the bottom of the chamber, using only one photomultiplier tube, for a source position directly above the tube, and for other angular positions. Also shown is the expected response from the sum of three tubes, spaced 120°. The relatively constant response with increasing distance is attributed both to the use of a high quality specular finish aluminum reflector on the inner walls of the scintillator chamber, and to the fact that liquid scintillators are, as a class, quite transparent to their own light emissions. This feature favored the choice of liquid scintillator over the use of plastic scintillator, which has an absorption length of the order of 50 cm. for its emission, compared to several meters for the liquid. The NE211 has also a somewhat higher light output than most plastics, provided it is purged of dissolved oxygen. A special "bubble tube" was built into the tank for this purpose, and dry nitrogen was bubbled through the liquid for 30 minutes prior to sealing.

B. Electronics and orientation systems. The electronics used for the experiment is shown in block diagram in Figure 3. The essential functions are straightforward. If the height of a given pulse corresponds to an energy $15 < E < 330$ Kev deposited in the central NaI crystal and if an anticoincidence pulse from the NE211 liquid scintillator "guard" channel does not occur within a resolving time of 250 nanoseconds of the given pulse, the pulse height is digitized and telemetered. In addition, the occurrence of the pulse is registered and telemetered as an event in the "low level singles" rate. If a guard pulse does occur within 250 Ns, the pulse is not pulse height analyzed and is registered only in the low level singles rate. In this way, the difference between the low level singles rate and the rate of PHA events measures the effectiveness of the anticoincidence system. (It was found during flight that the anticoincidence system lowered the total PHA rate by nearly a factor of 2.) If $E > 350$ Kev, the pulse is not digitized and is telemetered only in the "high level singles" rate, and finally, if $E < E_{min}$, the event is completely rejected. The digitizing process consists of converting the pulse height to a pulse of fixed height but of a time length proportional to the initial pulse height. The pulse is then used to gate the output of a 1 Megahertz quartz oscillator circuit, thus giving a string of 1 Megahertz pulses, the length of the string (and thus the number of pulses) being proportional to the original pulse height. The number of pulses is then counted by appropriate registers and formed into a binary word, composed of a sync bit plus 5 data bits, and then telemetered to a ground station at a bit rate of 1580 Hertz. Twenty seven channels were used to cover the energy range 15-330 Kev, corresponding to a width of ~11.7 Kev per channel.

In addition to the low level and high level singles rate, the guard event rate (all events for which more than ~30 Kev of energy was left in the liquid scintillator) was monitored, for use in correcting for dead time due to accidental coincidences. Each was scaled down to a rate of a few per second and sampled sequentially so that all three could be telemetered on a single subcarrier.

Auxiliary electronics included that for two "crossed" magnetometers (one digitized and one analogue), a gravity "zenith" sensor in the form of a low friction potentiometer (digitized) and a digitized temperature sensor. The two magnetometers served to uniquely determine the orientation of the experiment with respect to the local magnetic field, while the zenith and temperature sensors provided checks on experiment attitude and thermal behavior.

III. THEORETICAL BASIS OF THE DETECTOR

In order to register an X-ray event in an experimental system, it is necessary that the X-ray interact in some manner with the system. One must then know the response of the system to this interaction, and the details of its eventual conversion to usable data.

A. Fundamental interactions of photons (10-500 Kev) with matter. There are two principal types of interactions with matter which are of interest for X-rays of energies 10-500 Kev. These are Compton scattering and photoabsorption. The relative importance of these processes at a given energy is chiefly a function of the atomic number of the material in which the interaction occurs.

The attenuation of a beam of X-rays due to photoabsorption is a truly exponential process, since photoabsorption is catastrophic, i.e. the photon does not survive the interaction. We can then write

$dN/N = -\mu_p(E)\ dx$ and hence $N = N_0 \exp(-\mu_p(E)\ x)$.

$\mu_p(E)$ is called the photoabsorption coefficient and is strongly energy dependent. In the case of Compton scattering, we may also consider the attenuation to be exponential if we consider an initially well collimated beam of X-rays. Then, although the photon does not catastrophically disappear due to the interaction, its direction of propagation changes, and it is still removed from a collimated beam. Therefore, at least for thicknesses x such that $\Delta N/N$ is fairly small, we can also consider Compton scattering as an exponential process, since the probability of multiple scattering is small in such cases. We therefore may define an attenuation coefficient for Compton scattering, $\mu_c(E)$, thus $dN/N = -\mu_c(E)\ dx$ and $N = N_0 \exp(-\mu_c(E)x)$. The total attenuation coefficient for both processes is then given by

$\mu_T(E) = -\mu_c(E) + \mu_p(E)$.

We now consider the details of these two mechanisms.

In the process of photoelectric absorption, the X-ray interacts with the atom as a whole. The total energy of the photon is absorbed by the atom, and an inner orbital electron is ejected from the atom. The atom rebounds, conserving momentum, and the ejected electron carries away most of the available kinetic energy. Other electrons "fall in" to fill the vacancy of the inner orbit, and radiate a line spectrum of lower energy photons as they change energy states. Assuming the energy of the ejected electron is then progressively absorbed by the detector material in ionization and radiation losses, and assuming the line spectrum of photons emitted as above is absorbed by the material via other similar photoelectric processes, then the total initial energy of the X-ray is absorbed by the detector material. (There is, in general, some small probability that some of the line spectrum of "secondary" photons will escape the detector, and corrections must be applied accordingly.) The attenuation coefficient for the photoelectric effect is strongly dependent upon the atomic number Z of the material as well as upon the photon energy $h\nu$, and to a very crude approximation[8],

$$\mu_p(E) \propto Z^4/h\nu^3 .$$

In the Compton scattering process, one can consider that the photon interacts with one of the orbital electrons in a two body collision process. Both the electron and the photon rebound, conserving both energy and momentum, and the photon energy decreases in the process. One may use classical (relativistic) physics to describe the interaction, and may show that the energy $h\nu'$ of the photon after collision is related to the energy $h\nu_0$ before the collision by

$$h\nu' = h\nu_0/(1 + \alpha\ (1-\cos\ \theta)) \qquad (1)$$

where $\alpha \equiv \dfrac{h\nu_0}{m_e c^2}$, the ratio of the initial photon energy to the rest mass energy of the electron, and $\cos\ \theta$ is the angle between the directions of the initial and final photon momenta. The maximum loss of energy to the detector of a single Compton interaction occurs for a rebound angle of 180°, and is $\Delta h\nu_{max} = h\nu_0 \left[\frac{2\alpha}{1+2\alpha} \right]$ which value is often called the "Compton Edge". Thus a single Compton scattering process cannot cause the entire photon energy to be absorbed in the detector material as is the case with photoabsorption. Since the photon "survives", one can speak of both an attenuation coefficient for removal of the photon from a beam, and an "energy absorption" coefficient characterizing removal of energy from the photon beam, via the energy given to the electron with each Compton scattering process. The former is often called the "attenuation coefficient", and the latter the "absorption coefficient". The attenuation coefficient becomes identical with that for Thomson scattering at $h\nu_0 << m_ec^2$, and decreases slowly with increasing energy, while the absorption coefficient rises to a maximum near $h\nu_0 = m_ec^2$ and then decreases, as might be expected from purely classical collision calculations. Since the Compton process involves interaction of the photon with a single electron, and does not really involve the binding energy of the electron (so long as $h\nu_0 >>$ binding energy), the coefficients for Compton processes depend upon the number of electrons n per gm cm^{-2}. n (gm cm^{-2}) goes as Z/A, and Z/A $\approx$ 1/2 for all elements except hydrogen, for which Z/A $\approx$ 1. Thus the Compton attenuation and absorption coefficients at a given energy are nearly independent of the material.

There are a number of other possible interactions of X-rays with matter, nearly all of which are believed unimportant with respect to photoabsorption and Compton scattering at the energies being considered. One which may be significant is Rayleigh scattering, which is of course effective for photons of a few ev as well as several Kev. In this process, the orbital electrons respond to the varying electric field of the photon, and as a consequence, accelerate and re-radiate some of the incident energy. At 10 Kev, the wavelength of the photon is of the order of an Angstrom, which is characteristic of the size of the atom. Hence the electrons "feel the same field" as a function of time, and radiate coherently. As with Compton scattering, the full energy of the photon is not lost in the collision.

B. The Response of NaI(Tl) to photons of 10 to 500 Kev. In view of the above interaction processes, it appears desirable to have the photoelectric process predominate in a detector, since the entire photon energy can be absorbed making possible a more nearly unambiguous determination of the energy. In order for this to occur, a high Z detector is necessary. Thallium activated crystals of sodium iodide (principal absorber-Iodine, Z=53) are widely used for X-ray detection, both due to the high cross-section for photoabsorption for X-rays of energies up to several hundred Kev, and because it is a rather efficient scintillator, i.e. the material emits visible light when struck by photons and other particles. The absorption coefficients for the interaction processes discussed are shown in Figure 4. It may be seen that the photoabsorption process is dominant below 300 Kev, whereas Compton scattering is more important from 300 Kev up to several Mev. The light emission from sodium iodide crystals has a characteristic decay time of approximately 250 nanoseconds, with peak output at 4150 Angstroms. The output in visible photons per Kev of incident energy is of the order of 30. Linearity of the crystal is quite good[9], the light output per Kev being about 15 percent higher near 20 Kev than at 300 Kev, and changing slowly between these two values. The change in output with temperature changes is believed small.

Measurements in the range 30 to $\sim$60 Kev must be corrected for the "Iodine Escape" effect, i.e. the crystal is somewhat transparent to the K X-rays emitted when orbital electrons radiate and fall in to fill the vacancy created by the ejected electron during a photoabsorption. Axel[10] and others have investigated this problem, and Axel gives the escape probability for good geometry

$$P_{escape} = (.875)\ (.84)\quad 1 + r(\cos\theta)\ \ln\left(\frac{r\cos\theta + 1}{r\cos\theta}\right) \qquad (2)$$

where r is the ratioof the photoabsorption coefficients in NaI(Tl) at the "K edge" of 28.4 Kev, to that of the energy considered, and $(\pi-\theta)$ is the angle of incidence with respect to the vertical. Meyerhoff and West[11] have found experimental results which are in essential agreement with the above formula. The escape probability is the largest for low energies, since photoabsorption is likely to occur closer to the surface in this case. The probability of escape at 30 Kev is $\sim$30% for "good" geometry (i.e. X-rays incident at a point several absorption lengths from other edges) with near vertical incidence, and drops to 15% at 60 Kev. The photoabsorption length $X_p \equiv 1/\mu_p$ at 28.4 Kev is $\sim$.5 millimeter, hence our crystal should satisfy the "good" geometry condition at all points more than a millimeter from the edges, or at $\sim$97% of its area. The escape process then dictates that primary X-rays losing 28.4 Kev of energy then register as events in lower energy bins, thus there are actually two corrections for some of the channels, the first a correction for X-rays lost to a lower energy bin by the escape process, and the second a correction for X-rays ending up in the given bin due to escape processes at a higher energy. The total correction therefore depends upon the shape of the spectrum as measured at the detector.

C. The conversion of visible light into a usable electronic signal. In order to quantitatively measure the light output from a NaI(Tl) crystal, it is convenient to optically couple a photomultiplier tube to the crystal in order to utilize the high gain-low characteristic noise features of a photomultiplier tube. In the absence of saturation effects, the charge collected on the anode is then in principle closely proportional to the initial X-ray energy. Because of the relatively inefficient conversion of photons of X-ray energy to "visible" photons in even the best of scintillators, however, significant "broadening" ultimately occurs in the conversion to an electronic signal. In a well designed experiment, this broadening is chiefly due to statistics, and it is of some interest to consider the losses at each step. The visible photons produced in the crystal ultimately must pass from the crystal (refractive index · 1.67) through the optical windows of the crystal and the phototube. If the latter are glass, (refractive index is $\sim$1.5) some 65% may be lost due to internal trapping in the crystal,[42] i.e. rays whose angle of incidence at the NaI-glass interface is greater than the critical angle, (approximately 64 degrees). Assuming an initial crystal efficiency of 30 ev/visible photon only 9 photons/Kev reach the photocathode. A further reduction results from the low efficiency of the photocathode of the tube, typically 15-20%. Thus only about 1.5 photoelectrons are obtained per Kev of incident energy. If one takes a 22 Kev X-ray emission line, incident on the crystal, the number of photoelectrons emitted per X-ray is of the order of 30, $\pm$ 30, assuming Poissonian statistics. Thus the energy measured by the PM tube will not appear to be a well defined line, but a broad peak, whose width is some 40 to 50% of that of the position of the peak in this case. This effect is quite well understood, however, since the width of the peak is very nearly proportional to the square root of the energy, and corrections can be applied if a few calibrations have been made. Figure 5 shows the spectrum of Cd^{109} incident on the 11.4 cm diameter by 3 cm thick NaI(Tl) crystal used in the experiment, viewed by a 5" PM tube with the PHA performed by a 200 channel multichannel analyzer. The two peaks correspond to the two emission lines of this isotope, at 22 and 87 Kev. The "resolutions", i.e. the width of the peak at half its maximum, divided by the position of the peak, X 100%, are 50% and 25% respectively for the 22 Kev and 87 Kev lines with the crystal-phototube combination used in the experiment.

IV. SUMMARY OF FLIGHT

A. Preflight calibration. Preflight calibration of the experiment consisted of establishing the precise relationship between channel number and X-ray energy, and of determining the angular response of the detector. Energy calibration is quite straightforward, one need only position various microcurie strength sources in front of the detector. Figure 6 shows one such calibration, using a Cd^{109} source, as viewed by the flight electronics.

Determination of the angular response of the telescope to X-rays incident through the forward aperture was done by setting up millicurie strength sources at distances of several meters from the detector, and measuring the flux received as a function of the angle between the source direction and the telescope central axis. Angular measurement was provided by a very accurately calibrated 30 inch diameter aluminum protractor in conjunction with a simple sighting device. Although it was somewhat difficult to optically ascertain the position of the telescope for zero angle, relative angles were measured to within a quarter degree, with errors non-cumulative. Figure 7 shows the angular response determined for the energies 22, 87 and 125 Kev. It can be seen that they are essentially identical, as expected from the thicknesses of Pb and Sn which define the angle through their high opacity to X-rays of energies below 300 Kev.

B. <u>The flight.</u> The flight was launched at 0430 UT (2230 CST), 2 May 1967, from the balloon base of the National Center for Atmospheric Research near Palestine, Texas. The telescope was positioned at a fixed angle of 5°, and was rotated in azimuth by a line twister with period of approximately 11 minutes. The balloon reached a float altitude of ~ 4.6 gm/cm^2 about 2-1/2 hours later. Figure 8 shows averaged counting rates for two representative energy channels, 3 and 5, covering 23.4-35.1 Kev and 46.8-58.5 Kev respectively, for several interesting hours of the flight. The period during which the sources in the Cygnus region were to be expected was from 0900 through 1400 UT, as is suggestive by the increase in counting rate during part of that time. The instrument was recovered from a pasture near Albany, Georgia; the post-flight calibration agreed with the preflight calibration within the statistical limitations. Temperature changes during the flight were less than [illegible]°C, due to containment of the experiment within a heated pressurized gondola.

V. ANALYSIS OF THE DATA

A. Expected response of the detector to a point source on the celestial sphere. In order to ascertain the true rate of source flux for a particular source given the counting rate as a function of time, one must first determine the "response" of the instrument in the direction of the source as a function of time, i.e. the question is asked, "What fraction of the total area of the detector can be seen from the source position at a given time?" This involves some straightforward solid geometry and is treated in Appendix B. Briefly, the inputs to the response function are the following:

1. Universal time. This was determined via the simultaneous recording of WWV on the second channel of the audio tape recorders recording the telemetry.
2. Magnetic azimuth. Two crossed magnetometers were on board. The continuous transmission of their outputs (one digital, one analogue) provided a unique determination of the azimuth with respect to the direction of the horizontal component of the local magnetic field. The direction of the local magnetic field was provided from aircraft navigational maps of the trajectory area.
3. Balloon latitude and longitude. This information was furnished by the NCAR staff, based on aircraft-reported positions throughout the flight. The latitude changed by less than one degree throughout the entire flight. Longitude changed from 96 degrees to 84 degrees.

In order to facilitate computations of the response function by computer, the flight trajectory was divided into 27 zones, each zone having its own characteristic average latitude, magnetic correction figure, and balloon exit time. A few examples are given in Table 2. It is clear from the table that the changes in the three quantities are small between adjacent zones. Since the changes in longitude tended to be somewhat larger from zone to zone, and since a one degree change in longitude is capable of changing the positions of the peaks of the response function by nearly 4 minutes, the computer program used a "continuously changing" longitude, i.e. each succeeding calculation of the response function (at 12 second intervals) used a new longitude value, estimated by linear interpolation between known positions at known times, as per the NCAR data. Figure 8 shows Eff(t) for the 4 sources.

B. Separation of sources from the background. Figure 9 shows a map of the Cygnus region, showing the positions of the four sources X-1, X-2, X-3 and X-4 as determined by rocket measurements. Also shown is the FWHM of the detector as projected on the celestial sphere. It is evident that the FWHM is comparable to the angular separation of the sources, and there is thus an inherent difficulty in resolving them. This difficulty is almost a fundamental one in balloon-borne X-ray detectors, due to the requirement of a large area detector, for reasonable statistics, together with a shield of reasonable cost, weight and effectiveness. The detector of Haymes[12] has a comparable FWHM ($\sim 24°$); the FWHM of the Overbeck detector[13] is somewhat better ($\sim 8.4°$). In our particular experiment, we can, however, eliminate the contributions of X-2 and X-4 from the picture by considering the time interval 0920 to 1120. In this interval, the contribution of X-2 and X-4 are negligible, whereas half the total exposure to X-1 occurs during this time interval. In a later section, we shall estimate the contribution of X-3 to the counting rate by a perturbation technique, and will find that the upper limits to the flux from X-3 are a factor of 8 to 10 down from X-1 in essential agreement with Overbeck. We therefore shall ignore any contributions from X-3, X-2 and X-4 in the analysis to follow.

In situations where one has a really good signal to noise ratio, the extraction of the signal can be quite straightforward. For example, in the case of an idealized moon based X-ray telescope, the only background would presumably be due to a small primary cosmic ray flux, and a small diffuse X-ray background. Rather good S/N ratios could then be expected and by suitably small opening apertures, one could presumably neglect the background completely. The flux could be very simply determined by, for example, taking only data for those times when the response function was, say greater than 90%, and calling this the source flux.

However, in the case at hand, the "signal" is at best only half the "noise", and it is only this good for a few of the lower energy channels. At higher energies, the signal rapidly drops to a few percent of the noise. Again, this situation is common in greater or lesser degree to all balloon-borne detectors, although as the technique of shielding becomes better understood, the "background" is being reduced. A very useful technique for dealing with the poor signal to noise ratio is the following, due in part to Overbeck. We assume that the source and background are <u>constant</u> in <u>intensity</u> for the period of observation, and then write the following simple equation:

$$(R_{total}(t) - R_{BG})/Eff(t) = R_{source} \tag{3}$$

$R_{total}(t)$ represents the actual measured counting rate, R_{BG} is the background rate, R_{source} is the source rate, and Eff(t) represents the fraction of the detector area which is "illuminated" by the source. $R_{total}(t)$ and Eff(t) are of course time dependent, as indicated. A simple re-arrangement gives

$$R_{total}(t) = R_{source} \cdot Eff(t) + R_{BG} \qquad (4)$$

which is a simple linear equation in $R_{total}(t)$ and Eff(t) of the form

$$Y = AX + B.$$

Thus, if one plots the counting rate versus the response function, the result should be a straight line, whose slope is the source flux, and whose "y" intercept is the background. Figure 10 shows a typical result of such a plot for channel 5 (46.8 - 58.5 Kev); only points such that Eff(t) > .1 have been used in this case. A few error bars are indicated in Figure 10 representing one standard deviation for the raw counting rates. Each plotted data point represents 100 to 150 events, and only corrections for electronics dead ti[illegible] have been made to the data shown.

In view of the statistical scatter of the points in Figure 10, it is not at once clear how to best draw a straight line through the data. One possibility which has been used in this case by other workers[14] involves a least squares fit to the data. In this case, the criterion for best fit is the following. Suppose the "best" line to be represented by R(t) = A·Eff(t) + B. Then if we write a similar expression for each set of points (R_j, Eff_j), we have $r_j = R_j - A \cdot Eff_j - B$ where r_j is usually called the residual. A simple least square fit requires that $\sum_j r_j = 0$, further, that $\sum_j r_j^2$ be a minimum. The derivation[43] then gives the result that

$$R_{BG} = \frac{U_3\,U_5 - U_2\,U_6}{U_1\,U_5 - U_2^{\,2}} \tag{5}$$

and

$$R_{source} = \frac{U_6 - R_{BG}\,U_2}{U_5} \tag{6}$$

where U_1 is the number of data points N considered in the analysis.

$$U_2 = \sum_{j=1}^{N} Eff_j \quad , \quad U_3 = \sum_{j=1}^{N} R_j , \quad U_5 = \sum_{j=1}^{N} Eff_j^{\,2}$$

and

$$U_6 = \sum_{j=1}^{N} Eff_j\, R_j \; .$$

Figure 10 shows a "best fit" line obtained in this matter. Evidentally, because of the requirement that $\Sigma\, r_j^{\,2}$ = minimum, a simple least squares fit weighs points with large residuals more heavily than points with small residuals. However, if we assume that the distribution of points in Figure 10 is largely statistical (the distribution does approximately obey Poissonian statistics), then points with large residuals are actually statistically less likely than points with small residuals, and therefore should be weighed less heavily than points with small residuals. A technique which will accomplish this is a <u>weighted</u> least squares fit, where we now require the condition

$$\sum_{j=1}^{N} w_j\, r_j^{\,2} \text{ be a minimum.}$$

The statistical scatter of the points in Figure 10 suggests that perhaps w_j should be the probability of having a deviation r_j, if the "true" value lies on the best fit line. If we assume that the counting rate obeys Poissonian statistics, one may show[8] that the probability P_x of observing a rate X is

$$P_x = \frac{m^x}{x!} \quad e^{-m}$$

where m is the mean rate. For large m, this distribution is well approximated for our purposes by the "normal"distribution,

$$d\,P_x \;\alpha\; \frac{1}{\sigma}\;(e^{-(x-m)^2/2\sigma^2})\;dx \tag{7}$$

where σ is the standard deviation and equal to $\sqrt{m}$. This expression facilitates somewhat the necessary machine programming. If, then, we observe a mean rate R; then for a given measurement R_j, with a residual r_j, the probability of observing that residual is evidentally proportional to

$\frac{1}{\sigma}\; e^{-}\,(r_j^{\,2}/2\sigma^2)$ with $\sigma = \sqrt{R}$. For the purposes of computing the probability, the raw 30 second counting rates are used, before any dead time or other corrections are made. The technique then involves letting

$$W_j = \frac{1}{\sigma}\; e^{-r_j^{\,2}/2\sigma^2}$$

thus we require

$$\sum_j r_j^{\,2}\; e^{-r_j^{\,2}/2\sigma^2} \quad \text{be a minimum.}$$

In order to properly evaluate the exponential, one must know the true value, which in fact is the quantity in question. A technique which works very nicely in this case is to first determine a simple least squares fit (i.e. $W_j = 1$ for all j), then use this line to calculate the residuals. These residuals are then used to calculate the W_j for the expression above. A new best fit line is then computed using the weighting technique, new residuals computed, and the process repeated as often as necessary. Hopefully this process will converge, if the initial approximation is good enough, and in fact it does converge. Figure 11 shows the results at various stages of a 20 cycle iteration. It is believed that this technique is somewhat superior to a simple least squares fit of the data, since it does not weigh points with large residuals (statistically less likely) as heavily as those with small residuals (statistically more likely), whereas the reverse appears to be true for a simple least squares fit, as discussed above. The equations which finally result are as follows[43]:

$$B = (U_3' \; U_5' - U_2' \; U_6') \;/\; (U_1' \; U_5' - U_2'^{\,2}) = R_{BG} \qquad (8)$$

and

$$A = (U_6' - B\, U_2') \;/\; U_5' = R_{source} \qquad (9)$$

where

$$U_1' = \sum_{j=1}^{N} W_j \; , \; U_2' = \sum_{j=1}^{N} Eff_j \, W_j \; , \; U_3' = \sum_{j=1}^{N} R_j \, W_j$$

$$U_5' = \sum_{j=1}^{N} (Eff_j^{\,2}) \, W_j \; , \; U_6' = \sum_{j=1}^{N} Eff_j \, R_j \, W_j$$

On Figure 10 is drawn a line corresponding to a fit using the above technique.

Recalling that the signal to noise ratio is really not very good for the data, it is of some importance to ask how well we really know the "noise" or background. The AX+B" technique gives a unique value for the background, for example, but one can also learn something of the background by observing the counting rate of the detector for times when there are no known sources in the field of view. If these two determinations agree within error limits, then it is likely that we know the background rather well. Figure 12 shows the time profile for several channels of the 5 minute averaged counting rates for periods when Eff(t) for Cygnus X-1 is less than 7%. (The period where no background data is shown represents times when Eff(t) for Cygnus X-1 does not drop below 7%). Shown for each channel is a dotted line bridging the "blank" space and which represents the background value used for the Cygnus X-1 determination. Also shown is the background value obtained from the "AX+B" technique. In general, it was found that the background values from the "AX+B" technique were somewhat higher than one would expect from looking at the rates before and after passage of X-1, especially for the lower channels. Higher energy channels, with poorer signal to noise ratios, tended to give "AX+B" backgrounds which were in better agreement with the rates obtained by interpolation perhaps because the signal flux itself was actually smaller. The cause of the disagreement for the lower channels is not clear, but due to the uncertainty, it was decided to use the background obtained by manual interpolation between the levels observed before and after passage of the source. This choice would seem to have better statistical support, since some 2-1/2 hours of background data was recorded before and after the passage of the sources, whereas, by definition, background data (data at low efficiences) is not used in the AX+B fit. In this case we assume in the calculation that "B" is known, and determine the source rate "A" via Equation 9.

In comment on the technique of fitting a straight line to the plot of count rate versus the response function, it is believed that this technique uses a maximum of the available data for the source considered. In practice, however, the data used in these determinations has been restricted to points for which Eff(t) is greater than 10%. Inasmuch as the source rate is seen by Equation 3 to be inversely proportional to the value of Eff(t), a small error in the counting rate for 10% response tends to multiply the percentage error by a factor of ~10 as far as the source flux is concerned. Also, small values of Eff(t) were more difficult to measure, even with millicurie strength sources, and Eff(t) drops rapidly with small increases of angle for large angles. Hence values of Eff(t) less than 10% are not regarded as as trustworthy as the larger values. Eff(t) tends to be of the order of 40 to 100% for most of the duration of the observation period, fortunately.

The fluxes as measured at the detector, for a source at the position of Cygnus X-1 (as given by Giacconi et al[3]) are shown for each channel in Figure 13. The weighted least squares fit plus "known" background was used to obtain these values. Only corrections for electronics dead time have been made for the data shown in the figure. The decrease in the measured counting rates below 40 Kev is attributed to the strong atmospheric absorption occurring in the low energy region, as will be discussed in the following sections.

C. Corrections for instrumental dead times, and for atmospheric and gondola absorptions. The total counting rate of the detector in the analysis region was of the order of 100 events per second, pulse height analyzed, which was ~50% of the maximum rate which the electronics was capable of telemetering, hence corrections for "dead" or "busy" times of the electronics were necessary. These were of the order of 20% and the relevant formulae are derived in Appendix C.

After instrumental dead times have been taken care of, one can begin to make corrections for the absorption by the approximately 4.5 gm/cm^2 of atmosphere above the balloon, by the 1 gm/cm^2 of gondola insulation, and the .1 gm/cm^2 of aluminum comprising the gondola window. In making these corrections, one must bear in mind that attenuation of an X-ray flux by an absorber is strongly energy dependent. Thus, since the widths of the energy bins used for analysis cover a range of from 12 Kev (at lower energies) to 48 Kev (at the high energy end), the total absorption for a given bin will somewhat depend upon the X-ray spectrum incident at the top of the atmosphere. In principle, this is a circular argument, for the spectrum in space is the object of the investigation. However, in practice, the "absorption factor" for each channel (i.e. the ratio of the flux at the top of the atmosphere to that at the NaI crystal) is really not very sensitive to the exact shape of the spectrum which one might choose, especially at energies above 40 Kev. Table 3 shows the absorption factors obtained for two power law fits and two exponential fits, whose parameters have been chosen to be somewhere near those which have been reported by other workers. It can be seen that the higher energies are really quite insensitive to the shape chosen, principally because most of the absorption in air above 40 Kev is done by Compton scattering processes, and attenuation(i.e. removal from a beam) by Compton processes is a slowly varying function of energy as may be seen in Figure 4. (Although the data in Figure 4 is for sodium iodide, the attenuation by the Compton process is nearly the same per gm cm^{-2} for all materials, as has been noted earlier.)

It is of some importance at this point to ask whether a celestial "point" source will still look like a point source when viewed through several gm/cm^2 of air, or whether the Compton scattering will appear to broaden the angular dimensions of the source. If the source should appear to be several degrees wide at balloon altitudes, for example, significant corrections to the Eff(t) values could become necessary. The importance of the "halo" effect is fundamentally dependent upon the angular distribution of photons scattered by the Compton process. Figure 14 shows the angular distribution for photons of initial energies of 50 and 200 Kev. The FWHM for the scattered flux is seen to be nearly 180 degrees at 50 Kev, and more than 100 degrees at 200 Kev. To a first approximation, one may therefore consider the flux which is Compton scattered from a thin atmospheric layer to be uniformly scattered over a solid angle of $\sim 2\pi$ steradians for 50 Kev, and ~ 2 steradians at 200 Kev. The fraction intercepted by the detector is of the order of $\Omega_D/4\pi$ for 50 Kev, and $\Omega_D/4$ at 200 Kev, where Ω_D is the FWHM of the detector ($\sim .1$ steradian). Since only 10-20% of the incident flux is actually Compton scattered, and considering the small fraction of this scattered flux which is intercepted by the detector, any "halo" of Compton scattered photons is sufficiently dim that it need not concern us.

The corrections for attenuation of X-rays in the ~ 1 gm/cm^2 of Ethofoam insulation and $\sim .15$ gm/cm^2 aluminum gondola window are straightforward except for a possible worry concerning significant collection or amplification of the Compton scattered flux by the telescope barrel. If we bear in mind again the near isotropic scattering of the Compton process at the energies of interest for this experiment, then ~half of the flux is absorbed by the barrel walls at every scattering. Simple estimates then predict that the additional flux collected due to "barrel" scattering is $<1\%$ at 50 Kev, and $<2\%$ at 300 Kev, again small with respect to other sources of error.

The final absorption factors for each energy channel are given in Table 4. These factors include corrections for atmospheric and gondola absorption, a correction for increasing transparency of the crystal at higher energies, an Iodine escape correction as discussed earlier, and finally, a small correction due to the energy resolution of the detector. The finite resolution for each X-ray energy leads to "spillover" into adjacent "bins" when the X-ray energy is near the edge of a bin. If the actual spectrum were constant with increasing energy, the spillovers would cancel since approximately an equal number of events would spill over from both directions. However, the spectrum for Cygnus X-1 measured at the detector was not flat as has been shown in Figure 13. An estimate of the corrections indicate they are small, (0 to 20%) thus correction was made only to first order, by assuming a rectangular peak shape of width equal to the FWHM, instead of the usual nearly gaussian shape. The correction for a given channel is then the difference between what spills over from that channel into adjacent channels, and what spills into that channel from adjacent channels. The effect is to make high count rates higher and low count rates lower.

VI. DISCUSSION OF RESULTS

A. <u>The spectrum of Cyg X-1/X-3.</u> The spectrum obtained for Cyg X-1/X-3 corrected to the top of the atmosphere is given in Figure 15. For $20 \leq E \leq 100$ Kev, the data can be fit by

$$dN/dE = 3.45\ E^{-(1.71 \pm .1)}\ \text{photons/cm}^2\ \text{sec Kev.}$$

For energies above ~100 Kev, the spectrum appears to steepen:

$$dN/dE = 950\ E^{-(3.1\ {}^{+\ 1.5}_{-\ .6})}\ \text{photons/cm}^2\ \text{sec Kev.}$$

Figure 16 shows the same data together with the data of other workers whose flights occurred on dates near May 3, 1967. It can be seen that there is relatively good agreement between the results of this work, those of Bingham[14], and those of Overbeck and Tananbaum.[13] The data of Haymes et al[12] seem to be consistently lower below 100 Kev and may be an indication of source variability, as will be discussed later. As with the present work, the spectrum of Haynes et al also becomes steeper above 100 Kev, by about a power in the exponent. The only other measurements above 100 Kev which are known to the author at this time are by Rocchia et al[15] who report measurements to 135 Kev. This data is not inconsistent with a steepening of the spectrum beyond 100 Kev.

While the data as described above can be fit by two power laws, it can alternatively be well fit by a single exponential. Figure 17 shows a plot of the differential energy flux as a function of energy for this experiment, and for other workers. The data of this work appears to fit a single exponential rather well over the energy range 20-200 Kev:

$$dI/dE = .46\ \exp\ (-E/[78 \pm 10])\ \text{Kev/cm}^2\ \text{sec Kev.} \qquad (10)$$

The e-folding energy of 76 Kev, if interpreted as KT, corresponds to a temperature of 9.1×10^8 °K. Haymes et al. obtain an e-folding value of 94 ± 1 Kev as an alternate fit to two power laws; however, their data does not appear to fit an exponential as well as does the data of this experiment; their ± 1 Kev uncertainty is clearly underestimated (e.g. Figure 17b). Since their fluxes below 100 Kev seem to be consistently lower than those of Overbeck and Tananbaum, Bingham, and this work, there is a suggestion that the spectrum of Cyg X-1/X-3 may be more exponential when the source is intense as was the case in May and less so when "dim".

B. On the variability of Cyg X-1. The question of the variability of Cygnus X-1 has been considered by various authors.[13,16,17] Inspiration for such a question is amply supplied by differences in the reported fluxes. Whether the variations are real can perhaps be inferred by a temporal plot of the fluxes in various energy intervals reported by various workers, as seen in Figure 18. The present uncertainty concerning the variability is suggested by the widths of the error bars compared to the differences in fluxes for various dates. Absolute measurements of X-ray fluxes are difficult to make with present instruments, since the signal is not large compared to the background for balloon borne instruments, and differences in analysis techniques can easily make a 25% difference in the flux. In this light, the reported measurements of Overbeck and Tananbaum[13] are particularly interesting, since the same detector and analysis techniques were apparently used on four consecutive flights. Their data reports a factor of ~2 increase in the flux from September 1966 to May 1967, followed by a decrease of a factor of ~2 measured in June of 1967. The results of the present work agree rather well with the high fluxes of Overbeck and Tananbaum for May 1967, as well as agreeing quite well with the data of Bingham whose instrument flew on the same balloon as this experiment. It is felt, therefore, that the flux was definitely high in May 1967, and that probably the flux may indeed have been lower in September 1966 and June 1967 as suggested by Overbeck. The other reported fluxes are suggestive of variations, but the analysis techniques presumably are somewhat different for each experimenter so that less importance must be attached to these differences.

Also shown in Figure 18 are the fluxes measured below 10 Kev by rocket experiments. There are few data points in this region, and so the apparent lack of correlation between these low energy fluxes and the balloon borne measurements may not be meaningful.

C. <u>The spectra of Cygnus X-2/X-4 and X-3.</u> Since the exposure of the detector to Cygnus X-2/X-4 has been shown to be well separated from that due to X-1/X-3 (e.g. see Figure 8), one can use the previously described weighted least squares techniques to determine the flux from the pair X/2-X/4. Determination of the background flux for Cygnus X-2/X-4 is somewhat more difficult than for X-1, since no background data is available before the pair comes into view (due to the strong presence of Cygnus X-1/X-3). Background data after transit of X-2/X-4 has therefore been used in the least squares fit. Figure 19 shows the fluxes measured for X-2/X-4, along with other available data on the pair. The error bars are much larger than for the measurements of X-1 by this experiment, reflecting the increased importance of the background uncertainty with the much weaker fluxes. It can be seen that the results from this work are not inconsistent with the estimates of Overbeck and Tananbaum[13] and the data of Rocchia.[15] The spectrum is evidentally quite steep at these energies.

The optical counterpart of Cygnus X-2 appears to be a faint blue binary[18] of magnitude $m_v \sim 14.5$. The spectrum of Cygnus X-2 over a wide frequency spectrum is shown in Figure 20 where it has been assumed that the balloon borne data (above 20 Kev) refers to a flux principally from X-2. Two possible exponential fits are shown in the figure; neither appears entirely satisfactory. A power law fit would be a straight line on this plot, apparently not all compatible with the optical identification.

As with Cygnus X-2, very little data exists for the source Cygnus X-3. The ASE group[35] measured fluxes at 2 to 10 Kev, and Rocchia et al[15] has published fluxes for energies above 20 Kev. With the exception of Rocchia et al, most workers have found only upper limits for this source above 20 Kev; the absolute flux is difficult to measure due to its proximity on the celestial sphere to the stronger source X-1. In the present work, the flux from X-3 is estimated by looking at the time behavior of the source flux (computed by the techniques already discussed), using an Eff(t) for Cygnus X-1 only. Since X-3 comes into view about a half hour later (e.g. Figure 8), a significant contribution by X-3 should cause the computed source flux for X-1 to <u>increase</u> as X-3 comes into view. Figure 21 shows the source fluxes for X-1 + X-3 as a function of time determined by the previously discussed computer techniques, using an Eff(t) for Cygnus X-1 only and a background determined from Figure 12. There may be a small increase toward the end of the time interval in one channel, consistent with a small contribution from X-3; however, a lower energy channel actually shows a decrease. In view of the size of the error bars, these variations can be interpreted as only upper limits for contribution from X-3. Figure 22 shows the upper limits from this work, together with the results of other workers. The data is clearly quite scanty, and more work needs to be done by telescopes of larger area, lower background, and smaller aperture angles.

In comment on the data present in Figure 21, there is a suggestion of an increase in the flux from X-1 during the early part of the observation.

The calculated flux (measured at the detector) between 23.4-35.1 Kev is 154 C/min in the time interval 1015-1044, and then drops to 87 C/min in the succeeding time interval. The difference is 5 times the expected uncertainty due to lack of knowledge of the background, which is the largest source of uncertainty in the source flux. The decrease corresponds to more than 3 standard deviat... if the variations in the background and source flux are Poissonian. Channel 4 shows no evidence of this "short term variability", however, so the spectrum of the apparent fluctuation may be fairly steep.

D. The diffuse X-ray background. In addition to the now well established presence of numerous discrete celestial X-ray sources, there has accumulated much evidence for the existence of a broad diffuse component of extra-terrestrial X-radiation.[19,20,21] Recent results by Gorenstein et al[19] in the energy range 1-10 Kev indicate near isotropicity at these energies, and a photon number spectrum which goes as

$$dN/dE \propto E^{-1.7 \pm .2} .$$

In the interval 20-100 Kev, Bleeker et al[20] finds a spectral index of $\sim -2.4 \pm .2$, while the data of Seward et al[22] fits a power law with a spectral index -1.6 between 4 and 40 Kev. The data of Metzger et al[23] suggests a power law with an index of ~ -2.5 (Ranger 3, detector extended) in the interval 100 Kev to 1 Mev, and the upper limits measured by Clark et al[24] are consistent with an index of ~ -2 for E > 100 Mev. In summary, the number spectrum for energies above 100 Kev seems poorly known, but may become steeper above 20-60 Kev. This steepening, if real, could have important bearing upon the nature of the generation mechanism for the diffuse background. It is therefore extremely important to attempt to measure the diffuse component in the region of this break, that is, 20-100 Kev.

Balloon borne measurements of the diffuse X-ray background are difficult to make, for, as is the case with flux measurements of discrete sources, measurements of the diffuse X-ray flux are fundamentally limited by the background produced by cosmic rays in the atmosphere and in the instrument itself. In the case of discrete sources, one need only require that this background remain constant while the source is being viewed. However, the near isotropicity of the diffuse extra-terrestrial flux makes observation of this flux from a balloon difficult, since the atmospheric background is also nearly isotropic. Several techniques have been used in an attempt to separate the extra-terrestrial component at balloon altitudes, and nearly all depend upon the behavior of the counting rate as the experiment reaches altitude. Bleeker et al[20] have carried out two balloon flights at substantially different geomagnetic latitudes (53°N and 25°N) in order to try to distinguish any flux due to bremsstrahlung by electrons precipitating from the radiation belts. A rotating disk alternately closed and opened the aperture of the telescope in an attempt to separate the "forward" X-rays from the total measured flux. The flux with "closed" aperture is subtracted from that with "open" aperture, and the remainder is interpreted as being due to an extra-terrestrial component plus an atmospheric component. For pressures of between 20 and 100 gm/cm^2, where the contribution from the extra-terrestrial component would presumably be negligible, they found that the log of the counting rate (principally atmospheric) decreases linearly with the log of the pressure. The assumption is then made that the atmospheric component will <u>continue</u> to decrease in this manner for pressures less than 20 gm/cm^2. This technique then predicts the contribution of the <u>atmospheric</u> component to the difference between counting rates of the "open" and "closed" configuratons, and the extra-terrestrial contribution is taken as the remainder of this difference.

Hudson, Primbscl and Anderson[21] used the difference in counting rates from two identical detectors, one pointed upward and one downward, flown simultaneously, to separate the forward component. The flux measured with the "up" detector was about a factor of 2 greater than that of the "down" detector near 30 Kev.

Brini et al[25] used a technique similar to that of Hudson et al and employed one "up" detector, one "down" detector, and one detector with the aperture "closed". In contrast to Hudson et al, however, these workers found a flux from the "up" detector which was smaller than that from the "down" detector, yet their results agree with those of Hudson et al to within a factor of two! This relatively good agreement of the finished data in spite of an apparently very serious disagreement in the raw data may be indicative of the immaturity of measurements of the diffuse component.

Figure 23 shows the counting rate as a function of pressure for a representative energy channel for this experiment. To a first approximation, there is a linear region on these log log plots of rate versus altitude similar to the linear region on the log log plots of Bleeker et al. If we assume that in the absence of an extra-terrestrial component, the counting rate would continue to decrease with pressure in such a manner; we may estimate the contribution of the extra-terrestrial component as the difference between the actual counting rate and the rate which one would obtain by extrapolating the straight line region to lower pressures. Figure 24 shows the resultant fluxes, in comparison with

Bleeker et al and other workers. The data of the present work can be crudely fit by a power law:

$$dN/dE \propto E^{-2.8 \pm 1.3}$$

which is consistent with the index of $-2.4 \pm .2$ found by Bleeker, but also scarcely inconsistent with the $-1.7 \pm .2$ obtained by Gorenstein et al at lower energies. If there is a steepening of the spectrum occurring near 20-60 Kev, much more accurate measurements than those presently available will need to be made to establish the energy at which the steepening occurs.

VII. MODELS FOR X-RAY GENERATION BY LOCALIZED SOURCES.

We now review the fundamental X-ray generation mechanisms which are considered likely for localized stellar sources of X-rays. Generation of X-rays is contingent upon the acceleration of charged particles, and in this case only electrons are important. Since the radiated power P by an accelerated charged particle goes as

$$P = 2/3 \; \frac{e^2}{c} \; (\dot{\vec{\beta}})^2 \text{ for } \beta \equiv V/C << 1$$

and

$$P = 2/3 \; \frac{e^2}{c} \; \gamma^6 \left[(\dot{\vec{\beta}})^2 - (\vec{\beta} \times \dot{\vec{\beta}})^2\right] \qquad (11)$$

for relativistic velocities[26], where $\gamma \equiv \frac{1}{\sqrt{1-\beta^2}}$, the power radiated is proportional to the square of the acceleration $\dot{\vec{\beta}}$. The electromagnetic forces on electrons and other charged particles are only dependent upon charge and velocity; however, the much smaller rest mass of the electron results in acceleration ~2000 times that of protons, for equal electromagnetic forces. For electrons and protons of equal kinetic energy, γ for electrons is ~2000 times that for protons (again due to the difference in rest masses) so that the denendence on γ in Equation 11 above further enhances the electron contribution for relativistic energies. In the first case below, we consider acceleration of an electron due to a magnetic field, either a field of spatial extent (synchrotron radiation) or that due to the electromagnetic field of a colliding photon (inverse Compton radiation). The second case considers the radiation produced due to acceleration of the electron in the field of an atomic nucleus. A third case considered is that of "black body" radiation, which is the thermal radiation emitted by a body when the body is optically thick for photons of the energy considered.

A. Synchrotron radiation. Synchrotron radiation, caused by the acceleration of electrons in a magnetic field is thought to be responsible for much of the emission observed from celestial point sources in the radio range. First observed in synchrotrons, the radiation is characterized by a high degree of polarization since the direction of the electron acceleration is always perpendicular to its velocity and to B. Thus the radiation viewed perpendicular to B is linearly polarized (electric field vector perpendicular to the existing B field). Viewed parallel to B, the radiation is circularly polarized and it is thus elliptically polarized between these two extremes. For $V/c \ll 1$, the emission is at ν_c, the cyclotron frequency:

$\nu_c = \frac{e B_\perp}{2\pi mc}$ where m is the rest mass of the electron, while for $V/c \sim 1$, the emission pattern becomes very pronounced in the forward direction, and higher harmonics are introduced. Schwinger[27] has investigated this theoretically, and Corson[28] and others have verified the results on synchrotrons. The average power emitted per unit frequency for an electron of total energy E is found to be

$$\overline{P}(\nu) = \frac{\sqrt{3}}{\pi^2} \left(\frac{e^2}{mc^2}\right) \frac{E}{R} F\left(\frac{\nu}{\nu_m}\right), \tag{12}$$

where

$$\nu_m = 3/2\ (E/mc^2)^2\ \nu_c \tag{13}$$

$R = \frac{mVc\gamma}{eB}$ is the instantaneous radius of the orbit, and $F\left(\frac{\nu}{\nu_m}\right)$ is a slowly varying function. The maximum emission per frequency interval occurs near $\nu = \frac{\nu_m}{5}$, with the half power points near $10^{-2}\ \nu_m$, and ν_m. Schwinger shows that for a circular orbit,

$$P_n = \frac{(4)\ (3^{1/6})\ \Gamma(2/3)\ \ e^2\ \nu_c^{\ 2}}{\beta\ C} \left(\frac{mc^2}{E}\right) n^{1/3} \text{ for } \nu \ll \nu_m \tag{14}$$

while for $\nu \gg \nu_m$ the spectrum decreases exponentially:

$$P_n = \frac{3^{3/2}\ \pi^{3/2}\ e^2\ \nu_c^{\ 2}\ n^{1/2}\ e^{-n/n_m}}{\sqrt{2}\ \beta\ C\ \ n_m^{\ 3/2}} \tag{15}$$

where Pn is the power radiated per unit frequency in the nth harmonic of ν_c, and Γ is the "gamma" function. The total power radiated is given by

$$\overline{P}(E) = 2/3\ \frac{e^2\ \nu_c^{\ 2}}{4\ \pi^2\ c} \left[\left(\frac{E}{mc^2}\right)^2 - 1\right]. \tag{16}$$

Morrison[29] gives the half-life for energy loss by synchrotron radiation as

$$T_{1/2} \sim 5.1 \times 10^8/B_\perp^2\ \gamma \text{ seconds} \tag{17}$$

where $B_\perp$ is in gauss.

Although synchrotron radiation is believed important at radio frequencies, the mechanism requires rather high energy electrons for emission of X-rays. For example in a 10 microgauss field, for $h\nu_m = 1$ Kev, electron energies of $\sim 10^{13}$ ev are required. The half life is seen by Equation 17 to go inversely as γ, thus problems of electron lifetimes may arise in connection with X-ray fluxes at higher energies. If one assumes a power law spectrum of electrons (e.g. cosmic rays), $dN/dE = K\,E^{-\alpha}$ and assumes that all synchrotron radiation for an electron of energy E occurs at $\nu = \nu_m$, then the X-ray number spectrum is also a power law:

$$dN/dE = K_1\ E^{-(\alpha+1)/2}.$$

Thus a power law is expected for X-rays if the generating electron spectrum is a power law.

B. Inverse Compton radiation. An electron will also radiate due to interaction with an electromagnetic field, such as that due to a starlight photon. If the electron is relativistic, and the photon of energy $h\nu \ll m_eC^2$, the interaction is often called an "inverse" Compton process. Although in this case, the electron transfers energy to the photon, instead of vice versa, the interaction can be treated simply as a Compton scattering process, merely by a transformation to the rest system of the electron. The photon energy in this system is then given by the expression:

$(h\nu)'_i = \gamma(h\nu)_i\ (1+\beta)$ for a headon collision, where γ, β refer to the velocity of the electron in the "lab" system. After the collision, the photon energy is given by the usual expression (Equation 1):

$$(h\nu)'_f = \frac{(h\nu)'_i}{1 + \alpha(1-\cos\theta')} \quad \text{where } \alpha \equiv \frac{(h\nu)'_i}{m_eC^2} \quad \text{and}$$

cos θ is the scattering angle, as discussed earlier in this work. If we suppose $\gamma > 10^3$, then $\alpha << 1$ and $(h\nu)'_f \simeq (h\nu)_i$ with merely a reverse in the momentum direction for a headon collision. Then the final energy of the photon in the lab system is given by

$$(h\nu)_f = \gamma(h\nu)'_f \ (1+\beta) \simeq \gamma^2 \ (h\nu)_i \ (1+\beta)^2$$

for a headon collision, where the sign in the parenthesis is again positive because of the change in the direction of the photon momentum in the rest system of the electron. We thus see that the final energy is approximately γ^2 times the initial energy, which is analogous to the energy dependence discussed earlier for synchrotron radiation (Equation 13) viz:

$$\nu_m = 3/2 \ (E/mc^2); \quad \nu_{cf} \simeq {}^2 \ \nu_{ci} \ .$$

As is the case fo synchrotron radiation, inverse Compton scattering gives a distribution of photon energies, since all collision angles are of course possible. Other expressions for the inverse Compton and synchrotron processes are rather similar also. Felton and Morrison[30] show that the radiated power is given by the expression

$P_c(\gamma,\rho) = 2.66 \times 10^{-14} \gamma^2\rho$ eV/sec where ρ is the energy density in eV/cm^3 due to photons. Like the corresponding expression for synchrotron radiation, the power radiated goes as γ^2. The ratio of the power radiated due to each process goes directly as the ratio of the energy densities:

$$\frac{P_s(\gamma,B)}{P_c(\gamma,\rho)} = 3/2 \ \frac{(B^2/8\pi)}{\rho} \quad . \tag{18}$$

For generation of photons of several Kev from starlight photons ($\sim$1 ev), γ's of 50 for the electrons are sufficient. For the 3 degree universal radiation,

γ's of $\sim 10^3$ are necessary.

C. Thermal Bremsstrahlung. A mechanism which does not require such high energy electrons for emission of a given energy X-ray is the thermal radiation or "bremsstrahlung" occurring due to acceleration of thermal energy electrons in the Coulomb field of the nucleus. If a plasma is optically thin at X-ray energies, that is, the absorption length $X_0 \equiv 1/\mu$ for the energy considered is comparable to (or greater than) the thickness of the plasma, then the continuum radiation from this process is given by[31]

$$P_B(\nu) = 5.44 \times 10^{-39}\, \bar{g}\,(\nu,T)\, \exp\left(-\frac{h\nu}{KT}\right)\, T^{-1/2} \cdot \sum_z n_e\, n_z\, Z^2 \text{ ergs/cm}^3 \text{ ster sec c/sec,} \qquad (19)$$

where n_e, n_z are the number densities of electrons and of ions with charge Ze, and $\bar{g}$ is the effective Gaunt factor. $\bar{g}$ approaches unity for $h\nu \gg KT$, and approaches $\frac{\sqrt{3}}{\pi}\, \ln\left[\frac{4KT}{.5h\nu}\right]$ at low frequencies. Note that the shape of $P(\nu)$ is nearly flat out to an energy $h\nu \doteq KT$ and then drops off exponentially for $h\nu > KT$. As KT is typical of the electron energy in the plasma, we see that this can be a fairly efficient generation mechanism--electrons of energy E can produce photons of energy $h\nu \lesssim E$. The total isotropic emission by this mechanism is given by

$$P = 1.44 \times 10^{-27}\, T^{1/2}\, \bar{g} \sum n_e\, n_z\, Z^2 \text{ ergs/cm}^3 \text{ sec.} \qquad (20)$$

We can estimate the half-life of the plasma for cooling by bremsstrahlung in the following manner. Suppose $n_e \cong n_z \cong n$, the total particle density, then $P = \frac{du}{dt} \cong (1.44 \times 10^{-27})\, \bar{g}\, n^2 \sqrt{T}$, where u = thermal energy density

of the plasma. But u = 3/2 n KT by classical kinetic theory, hence
$\frac{du}{u} \approx \left(\frac{1.44 \times 10^{-27}}{3/2 \sqrt{T}}\right) n \bar{g}$ dt $\approx$ dt/ $\tau_{1/2}$ whence $\tau_{1/2} = \frac{10^{11}}{n} \sqrt{T}$ in seconds. Thus the higher the number density, the faster is the cooling time by bremsstrahlung.

D. Black body radiation. When the number density in a plasma becomes so high that the plasma is no longer optically thin for photons of a given energy, the radiation approaches "black body" for that energy. The bremsstrahlung formulae no longer apply and the emission now goes as the surface area of the body and is given by the Planck function:

$$P(\nu) = 2\pi\nu^2/c^2 \left(\exp\left(-\frac{h\nu}{KT}\right) -1\right) \text{photons/cm}^2\text{sec} \quad \text{C/sec} \qquad (21)$$

The total power radiated is the integral of the above expression:

$$\bar{P} = \sigma T^4, \text{ where } \sigma = 5.67 \times 10^{-5} \text{ ergs/cm}^2 \text{ sec deg}^{-4}.$$

VIII. COMPARISON OF DATA WITH THEORETICAL MODELS

A. Cygnus X-1. The spectrum obtained for Cygnus X-1 has been shown in Figures 15, 16 and 17. We now consider the shape of the spectrum in the light of the generation mechanisms which have been discussed.

As has already been considered, the spectrum does not appear to be well fit by a single power law. Below 100 Kev, a power law with spectral index ~1.7 seems to fit adequately, while above 100 Kev, the spectral index steepens by about a power. This steepening of the spectrum above 100 Kev has also been observed by Haymes et al so is believed to be real.

At least one other source shows a spectrum somewhat similar to that of Cygnus X-1. The Crab Nebula (Tau X-1) is also a powerful X-ray emitter at energies up to 100 Kev and its overall energy spectrum also shows a break, although the break is from an exponent 1 to 2 and occurs at a much lower frequency[32] of ν 3×10^{13} C/sec in contrast to the steepening of the Cygnus X-1 spectrum at ν 2×10^{19} C/sec. Since the lifetime of an energetic electron is known to go inversely as its energy (e.g. Equation 17) under synchrotron loss, the steepening of these spectra is suggestive of the gradual loss of electrons energetic enough to produce radiation above the "break" energy. Kardashev[33] discusses the changes in an electron spectrum due to synchrotron radiation, and for the particularly simple case in which an electron spectrum of the form

$$N_e(E) = K\,E^{-\gamma}$$

is initially injected (and no further injection occurs thereafter) and the electron velocities are isotropic (i.e. all angles with respect to B), then the electron spectrum evolves with time and steepens at an energy

$$E_{break} = \frac{1}{b\,B^2\,t} \tag{22}$$

where $b = .98 \times 10^{-3}/(mc^2)^2$, B is in gauss, t is in seconds and E_{break} is in ev. The corresponding break in the synchrotron emission spectrum from these electrons occurs at

$$\nu_b = 3.4 \times 10^8/B^3\,t^2, \tag{23}$$

where t is in years and ν_b is in C/sec. The synchrotron spectrum at time t after the initial injection of the electrons is determined to be

$$I(\nu) \quad B^{\left(\frac{\gamma+1}{2}\right)} \quad \nu^{-\left(\frac{\gamma-1}{2}\right)} \tag{24}$$

for $\nu << \nu_b$ where $I(\nu)$ is the energy spectrum, and

$$I(\nu) \propto B^{-2} \quad \nu^{-\left(\frac{2\gamma+1}{3}\right)} \quad t^{-\left(\frac{\gamma+5}{3}\right)} \text{ for } \nu >> \nu_b. \tag{25}$$

For the Crab, the photon energy spectrum for $E < E_{break}$ has an index of $\sim .25$ corresponding to a $\gamma \sim 1.5$. The value of the photon spectral index predicted for $E > E_{break}$ via Equation 25 is then $(\frac{2\gamma+1}{3}) = 1.3$, which is close to the 1.2 actually found for the Crab. A break frequency of 3×10^{13} C/sec predicts $B \sim 2 \times 10^{-4}$ gauss, considering the known age of ~ 900 years for the Crab.

For Cygnus X-1, a photon energy spectral index of 0.7 for $\nu << \nu_b$ (i.e. $h\nu < 100$ Kev) gives a γ of 2.4 via Equation 24. Equation 25 then predicts a photon spectral index of $(\gamma+5)/3 = 2.5$ for $\nu >> \nu_b$ (i.e. $h\nu > 100$ Kev), which is consistent with the $3.1 \pm ^{1.5}_{.6}$ energy spectral index measured by this experiment for $E > 100$ Kev. If this mechanism applies, an estimation of the age of the source Cygnus X-1 can be made by assuming a magnetic field value of, say that calculated for the Crab. If we assume $B \sim 10^{-4}$ gauss, Equation 23 predicts an age of $t \sim 3$ years, almost certainly too short. If we try $B \quad 10^{-5}$ gauss, perhaps more reasonable, we find $t \sim 10$ years, again rather short but perhaps not entirely unreasonable, since the first observations of Cyg X-1 were made less than seven years ago. However, an optical upper limit (to be discussed later) has been measured for Cygnus X-1 which is clearly not compatible with the spectral index of 1.7 measured for energies of less than 100 Kev. Another "break" at lower energies is thus required. There may therefore be difficulties in the synchrotron hypothesis for Cygnus X-1. Nonetheless the model is attractive for its simplicity and a later observation of a shift of the break to a lower energy would appear to lend support to the hypothesis of a young source and a synchrotron mechanism.

Another alternative to be considered for the interpretation of the spectrum of Cygnus X-1 is that thermal bremsstrahlung may be the emission mechanism. This is somewhat more attractive from an energy point of view, at least, since X-rays of tens of Kev may be produced by thermal electrons with comparable energies as has been previously considered. The source Sco X-1, for example, is believed to be producing X-rays by a bremsstrahlung mechanism in the X-ray region since its energy spectrum appears to be an exponential and in fact an "acceptable" optical counterpart has been found by extrapolating the X-ray spectrum back to visible wavelengths.[34] It is therefore worthwhile to investigate this possibility for Cygnus X-1. As has been shown in Figure 17, the data of this experiment appears to fit an exponential rather well. Figure 17 also shows most of the rocket data known at this time. There appears to be considerable "scatter" of the rocket data, perhaps due to time variations of the source as discussed earlier in this work. However, the low energy data is not inconsistent with an extrapolation of the exponential fit to the data of this experiment. Little is known of this source at still lower X-ray energies; however, an important upper limit of $m_V \sim 15$ has been found for the visible flux from the optical counterpart of Cygnus X-1[46]. Figure 25 shows some of the presently available data for Cygnus X-1 over an extended range. Also shown is an exponential "fit" of $T \sim 10^9$ °K which is compatible both with the optical upper limit and with the data of the present work.

A bremsstrahlung hypothesis is attractive considering the evidence for variability of Cygnus X-1 as well. Overbeck and Tananbaum[13] and Lewin et al[45] have reported observing time variations in Sco X-1, whose spectrum in the X-ray region is apparently exponential; the optical counterpart[34] appears to show definite variability, and the corresponding radio object also may be variable.[37] Cygnus X-1 and Sco X-1 might therefore be similar objects. If so, Cygnus X-1 appears to be much hotter than Sco X-1 ($\sim 10^9$ °K as compared to 5×10^7 °K), and also apparently much hotter than Cygnus X-2 ($\sim 5 \times 10^7$ °K) although a single temperature for X-2 does not seem to fit both the optical and X-ray data. Cygnus X-1 may therefore be the hottest object yet discovered in the universe.

All evidence considered, it is believed somewhat more likely that the spectrum of Cygnus X-1 is more naturally fit by an exponential energy spectrum than by a power law number spectrum. One cannot at this date rule out the synchrotron mechanism, since it may well be that the source is a very young one, and that the break is indicative of a depletion of high energy electrons.

B. <u>Cygnus X-2/X-4 and X-3.</u> The energy spectrum for Cygnus X-2/X-4 measured in this experiment has been given in Figure 19. Figure 20 shows the flux over an extended range of energies, including the optical counterpart of X-2 measured by Kristian.[18] Also shown in Figure 20 are two possible exponential fits to the data; neither appears to fit both the X-ray flux and the flux from the optical object. There may therefore be difficulties in understanding the flux of X-2/X-4 as due to a simple single temperature bremsstrahlung mechanism over a large energy range. X-ray measurements are very scanty and subject to large errors for energies above 10 Kev, since the flux is rather low. In addition, there is a lack of sufficient data below 10 Kev. Clearly much more experimental work needs to be done on the X-2/X-4 question.

In contrast to Cygnus X-2, the optical counterpart for the source Cygnus X-3 has not been found, as far as as known at this date and the balloon borne measurements are quite uncertain as has been shown in Figure 22. Gorenstein et al[35] has examined bremsstrahlung ($T=7.4 \times 10^7$ °K) and black body fits ($T=2 \times 10^7$ °K) and concluded that either is an acceptable fit at low X-ray energies. However, the same paper by Gorenstein et al presents a spectrum for Cygnus X-1 which is quite similar to that of X-3, and the shape of this spectrum for X-1 does not appear compatible with fluxes measured above 20 Kev (e.g. Figure 16) for X-1. It must therefore be concluded that the spectrum for Cygnus X-3 is rather indefinite at this time and there seems little justification to consider arguments favoring a power law, exponential or other fit to the scanty data.

C. Agreement of the diffuse X-ray background with theoretical models. The measurements of this work concerning the diffuse X-ray background have been presented earlier (Figure 24). Figure 26 shows fluxes for a more extensive range of energies, as reported by Gorenstein et al[19] and by other workers.[20,21,23,36] Gorenstein et al report a spectral index of -1.7 ± .2 from 1 to 10 Kev. The conglomerate of data from Bleeker et al, Hudson et al., Bowyer et al and that of this work seems to be adequately fit by a spectral index of -2.5 ± .3 in the 20-100 Kev range. There thus appears to be a suggestion of a steepening of the spectrum somewhere in the neighborhood of 50 Kev, and if real, may help to sort out the possible theoretical models which have been suggested for the generation of the diffuse X-ray flux. The diffuse X-ray flux appears to be roughly isotropic in nature; Gorenstein[19] reports no anisotropy greater than 8% in 30 x 30 degree sampling areas, over galactic coordinates ranging from -90° to +90° in longitude, and -70° to +90° in latitude. This strongly suggests the possibility of an extragalactic origin for the flux.

Several models have been considered as production mechanisms for the diffuse X-ray background. Gould and Burbidge[38] suggested a superposition of unresolved galaxies, each with discrete sources such as those in our own galaxy, but the question remains as to whether our galaxy is normal or unusual regarding its X-ray emission. Only one external galaxy (M-87) has definitely been observed to be an X-ray emitter at present detection levels. Silk[39] has suggested that a sufficient increase in the X-ray luminosity of normal galaxies (due to discrete sources) arising from evolutionary effects could account for the observed flux, and that perhaps an abundant presence of sources whose X-ray spectra steepen (as with Cygnus X-1) may account for the apparent steepening in the observed spectrum. The inverse Compton mechanism has been considered by Felton and Morrison[30] as a generation mechanism for the diffuse background, using cosmic ray electrons colliding with both starlight photons and with the 3 degree "universal" radiation. For the galactic halo only, the shape of the calculated spectrum (photon spectral index of -1.7 below 100 Kev, and -2.2 above 100 Kev) is in essential agreement with the observed shape; however, the flux is too low by a factor of at least 20, assuming the principal photon density is that due to the 3 degree radiation. The contribution from the halos from all external galaxies are calculated to be even smaller than the contribution of our own halo, unless the typical external galaxy is much brighter in the X-ray region than our own. Brecher and Morrison[40] report that if evolutionary effects are included, a large portion of the observed diffuse X-ray flux may be explained by the "inverse" Compton scattering of the 3°K radiation off electrons in the intergalactic region, but only if the sources for injection of electrons into the region were much stronger in the past than at present.

The essence of the arguments above appears to be that agreement of theory with the overall spectral shape of the diffuse X-ray flux is not terribly difficult; however, models which predict a steepening near 10-100 Kev are rare and may have difficulties. Further, theoretical models which agree with the observed flux seem only to be obtainable by incorporating evolutionary effects, and the necessary assumptions for these evolutionary effects seem somewhat uncertain. The balloon borne measurements of the diffuse flux seem almost equally uncertain, as discussed earlier, and much work, both theoretical and experimental, needs to be done in order to understand this component of the extra-terrestrial X-ray flux.

APPENDIX A. DISCUSSIONS OF ERRORS

There are several possible sources of error in the computations for the flux values made in this analysis. They are itemized below, with estimates of the uncertainty introduced due to each effect.

A. Error in instrument azimuth. This can be due to alignment and/or magnetic deviation errors. The total angular error due to these effects is estimated at ~1 degree or less. The absolute change in Eff(t) can be 15-20% per degree; however, the constant rotation of the instrument almost cancels this out due to the symmetry of Eff(t) about its maximum. The change in the source flux R_s is therefore estimated to be ~3% or less due to azimuthal errors.

B. Error in zenith angle. The error in instrumental zenith angle is estimated at one degree or less, due to the rigid gondola frame and the carefully made alignment measurements. The error which this introduces in Eff(t) depends on whether the zenith angle of the source is greater or less than the telescope zenith angle of 5°. If we assume that the zenith angle of the telescope is actually, say 5-1/2°, then for times when the zenith angle of the source is greater than 5-1/2°, the effect is to increase the peaks of Eff(t) and decrease the valleys so that the apparent source flux appears greater. Conversely, for times when the zenith angle of the source is less than 5-1/2°, the peaks of Eff(t) are decreased and valleys increased, thus decreasing the apparent source flux. There is therefore partial cancellation since the minimum zenith angle for Cygnus X-1 is ~3° for the latitude at which transit occurred during the flight. A similar situation of course would prevail for a telescope zenith angle of less than 5 degrees. The absolute change in Eff(t) is ~10% for a one degree shift; partial cancellation allows us to estimate Δk_{source} as $\lesssim$ 5%, arising from this effect.

C. The uncertainty in the absorption factors is dependent upon the spectral shape assumed for the calculation of atmospheric absorption for each channel, and upon the exact altitude of the instrument package. The effect of the former gives a ~10% uncertainty for channel 2, ~5% for channel 3 and a negligible amount for higher channels. The uncertainty in altitude is ± .2 gm/cm^2 which gives errors of ~14% for channel 2, 6% for channel 3 and <4% for higher channels.

D. There are other possible sources of errors <5%, but the most significant uncertainty in this experiment stems from an imperfect knowledge of the background flux. Although the background was observed for ~2 hours before and after passage of all four sources, there is evidence that the background changed slowly during observation of the sources. Figure 12 has shown the 15 minute averaged counting rate in selected channels before and after transit of Cygnus X-1, for times when Eff(t) of Cygnus X-1 is <7% and that of Cygnus X-2 <50%. It can be seen that there is a limited but critical period of 75 minutes when no background data is available, and one must attempt to interpolate within this hour. It is herein that the uncertainty arises. The magnitude of the uncertainty in the background is of the order of 5 to 10 C/minute in each channel and the resulting uncertainties in the source fluxes are of the order of 5 to 30% depending on the value of the source flux measured for a particular channel.

The best estimates of the effects of the above errors are represented by the error bars in Figure 15. Since the background variations are apparently not Poissonian (statistical variations are ~ ± 5 C/minute), it is difficult to assess a probability for these error bars, but they are believed to represent the equivalent of a standard deviation.

APPENDIX B- DERIVATION OF THE RESPONSE FUNCTION EFF(t).

In order to compute the angle between a telescope rotating at approximately constant azimuth, and the direction to a particular celestial object, it is convenient to first calculate the azimuth and altitude for the direction in which the telescope is pointing, and the same quantities for the stellar object, then to determine the angle between the two directions given these quantities. For the telescope in this experiment, the altitude is constant at 5 degrees from the vertical, and we only need to calculate the azimuth, A_T. The azimuthal angle with respect to local magnetic north comes directly from the magnetometer data; if the probe is in the plane of the 5 degree tilt, then a maximum in the magnetometer output corresponds to magnetic north, a minimum to magnetic south. Assumption of a sinusoidal variation gives angles in between these extremes, and monitoring of the output of a magnetometer probe at right angles to the first resolves any ambiguity in East and West. (The variation is closely sinusoidal if drifts in telemetry voltage are small compared to the amplitude of the variations, over a period of a cycle). The azimuth with respect to celestial north requires knowledge of the deviation from north of the horizontal component of the local magnetic field, which is a fairly slowly varying function (changes by only ~6 degrees from Texas to Georgia) and can be determined to a sufficient accuracy from aircraft navigational maps of the area.

The azimuth of a celestial object can be determined by reference to a spharical triangle (below).

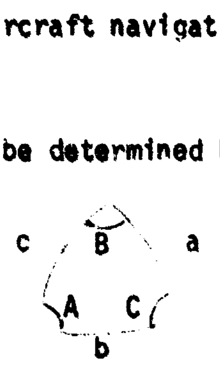

and by use of the law of sines for spherical triangles:

$$\frac{\sin a}{\sin A} = \frac{\sin b}{\sin B} = \frac{\sin c}{\sin C} \quad .$$

McLaughlin[41] shows that the following quantities form a spherical triangle:

$90° - \phi$ H.A. $90°-h$

A or
$360°-A$

$90° - \delta$

where

ϕ = astronomical latitude

h = altitude of the astronomical object

δ = declination of the object

H.A. = local hour angle of the object

A = local azimuth of the object

Use of the law of sines gives

$$\frac{\sin\,(90°-\delta)}{\sin(A)} = \frac{\sin\,(90°-h)}{\sin\,(H.A.)}$$

whence

$$\sin(A) \text{ or } \sin\,(360°-A) = \frac{\sin(90-\delta)\ \sin H.A.}{\sin\,(90-h)}$$

If the star is east of the great circle passing overhead of the observer, one uses sin A, whereas for angles west, one uses sin (360°-A). The hour angle H.A. is given by the relation

$$(H.A.)_{degrees} = (T_{sid} - RA) \cdot 15$$

where

T_{sid} = sidereal time at the position of observation, and

RA = right ascension of the object.

To a very good approximation, T_{sid} is given by the expression

$$T_{sid} = [1 + \frac{4}{1440}]\,[T_{GM} + \frac{37''}{3600}] + [RA_{\odot} - T_{Eph\ transit}] - \frac{\ell}{15}$$

where $RA_{\odot}$ is the apparent right ascension of the sun at transit of the prime meridian on the day considered, and $T_{Eph\ transit}$ is the Ephemeris time at the transit. Ephemeris time differs only by 37 seconds from universal time in 1967; conversion for other years is conveniently available[42], as are $RA_{\odot}$ and $T_{Eph\ transit}$. Finally T_{GM} is the Universal time in hours, and ℓ is the longitude in degrees.

The input of magnetometer voltage, balloon latitude and longitude, magnetic correction and Universal time then gives the azimuth and altitude, both for the telescope direction and for a given source at that time. We now can determine the angle between the telescope direction and that of the astronomical object by treating these directions as vectors, and taking a scalar product between the vectors. Figure 27 shows the coordinate system and a representative vector. We have: $\vec{R}_1 = R_{1x}\,\hat{i} + R_{1y}\,\hat{j} + R_{1z}\,\hat{k}$, where

$$R_{1x} = |\vec{R}_1| \cos h_1 \cos A_1$$

$$R_{1y} = |\vec{R}_1| \cos h_1 \sin A_1$$

$$R_{1z} = |\vec{R}_1| \sin h_1$$

where $\vec{R}_1$ points parallel to the telescope axis. We can write similar conditions for $\vec{R}_2$, the vector toward the astronomical object, and then take the scalar product. The result is:

$$\vec{R}_1 \cdot \vec{R}_2 \equiv |\vec{R}_1|\ |\vec{R}_2| \cos\theta = |\vec{R}_1|\ |\vec{R}_2| (\cos h_1 \cos h_2 \cos A_1 \cos A_2$$

$$+ \cos h_1 \cos h_2 \sin A_1 \sin A_2 + \sin h_1 \sin h_2)$$

where θ is the angle desired. $\vec{R}_1$, $\vec{R}_2$ are arbitrary and may be considered as unit vectors. All of the expressions above are believed to be exact, with the exception of that of T_{sid}, which is a linear approximation to the actual variation of sidereal time with Universal Time.

APPENDIX C - DERIVATION OF THE CORRECTION FOR DEAD TIME IN THE FLIGHT ELECTRONICS.

The dead time correction for a "simple" situation such as a Geiger-Müller tube asks the question, "What is the probability that after the occurrence of a given pulse, a second pulse will occur within a time τ of the first?" τ here is the characteristic "busy" or dead time occurring after each pulse. If the average registered counting rate is R_m, then the total busy time each second is given by $\Delta T = R_m \tau$. The measured rate is related to the "true" rate by the expression

$$R_{true} - R_{true} \cdot \Delta T = R_m, \text{ or } R_T = \frac{R_m}{1-\tau R_m} \; .$$

In contrast, the dead time correction for the flight electronics for this experiment must ask the question, "What is the probability that after one event has been registered, <u>two</u> more events occur within a time τ after the first?" That is, the logic is capable of storing a second event while reading out the first event, and significant live time is lost only when a third event comes along too soon. Thus for every situation in which two pulses are analyzed which fall within a time τ of each other, the electronics is "busy" for a time τ after the first pulse. The number of such events per second is $N = R_m(R_m\tau)$. The average position of the second such measured pulse is $\tau/2$ after the first, thus the average dead time per second is given by

$$T = (R_m \tau)^2/2$$

and we find

$$R_T = \frac{R_m}{1-(R_m \tau)^2/2} \; .$$

Actually there is a small but finite inherent dead time Δ after each registered event, during which time no second pulse is accepted. Δ is the time duration of a single binary bit, whereas τ is the time duration of an entire word of length 7 bits, thus $\Delta \ll \tau$. If we consider the inherent dead time Δ, then analysis similar to the above gives

$$R_T = \frac{R_m}{1 - \frac{R_m^2 \tau^2}{2} \left[\frac{\tau + 7/2\, \delta^2/\tau - 4\delta}{(\tau - \delta)} \right]} .$$

For the given experiment, τ = 5.7 milliseconds, and Δ = .8 milliseconds, thus R_T = 1.2 R_m for R_m = 100/second, a rate typical of that at altitude-- a correction of 20%. In contrast, the "G-M" tube type of correction would predict a correction of more than a factor of 2 for a 5.7 ms dead time and a rate of 100 C/second so there is a very significant difference between the "true" rates predicted by the two formulae, even though the maximum rates that can be measured are comparable:

$$R_{m\ max} = \frac{1}{\tau} \quad \text{for the "G-M" expression}$$

$$R_{m\ max} = \frac{\sqrt{2}}{\tau} \quad \text{for the logic of the flight electronics.}$$

TABLE 1

Positions and Intensities of the Cygnus Sources[19]

ASE Designation	R. A. (1950)	Dec. (1950)	Intensity*
Cyg X-1	$19^h\ 56^m\ 34^s$	35° 6'	.46
Cyg X-2	$21^h\ 42^m\ 48^s$	38° 11'	.45
Cyg X-3	$20^h\ 30^m\ 52^s$	40° 56'	.13
Cyg X-4	$21^h\ 9^m\ 11^s$	38° 33'	.05

* Counts/cm^2-sec, 2 < E < 5 Kev.

TABLE 2

Representative Parameters for Trajectory Zones

Zone No.	Latitude	Magnetic Correction	Balloon Exit Time
1	31.75°	8.0°E	0459 UT
2	31.75°	7.8°E	0520 UT
3	31.75°	7.5°E	0547 UT
4	32.00°	7.25°E	0638 UT
5	32.00°	7.00°E	0722 UT
6	32.00	6.82°E	0755 UT
7	32.13	6.65°E	0842 UT

TABLE 3

Atmospheric Absorption Factors at 4.5 mb

for Several Spectral Indices

Energy Interval	Power Law $-\gamma=1.65$	$-\gamma=1.8$	Exponential KT=60 Kev	KT=80 Kev
11.7-23.4 Kev	31.0	33.0	27.8	27.0
23.4-35.1 Kev	5.13	5.38	5.08	5.05
35.1-46.8 Kev	2.91	2.91	2.89	2.89
46.8-58.5 Kev	2.36	2.36	2.38	2.38
58.5-70.2 Kev	2.20	2.20	2.20	2.20

Agreement is better than 1% for energies above 70 Kev.

TABLE 4

Total Absorption Factors*

Channel	Energy Interval, Kev	$\bar{E}$	Total Absorption Factor
2	11.7-23.4	19	49.6
3	23.4-35.1	28	9.2
4	35.1-46.8	40	4.80
5	46.8-58.5	52	3.37
6	58.5-70.2	64	2.78
7	70.2-81.9	76	2.58
8-9	81.9-105.3	93	2.38
10-11	105.3-128.7	117	2.25
12-13	128.7-152.1	140	2.10
14-15	152.1-175.5	164	2.10
16-19	175.5-222.3	198	1.94
20-23	222.3-269.1	245	2.4

* For atmospheric depth of 4.5 mb, including 1" of Ethafoam insulation plus .020" of aluminum for power law spectrum, index $-\gamma=1.7$, including corrections due to resolution, iodine escape and increasing crystal transmission at high energies.

BIBLIOGRAPHY

1. Giacconi, R., Gursky, H., Paolini, F. R., and Rossi, B. B., 1962, Phys. Rev. Letters 9, 439.

2. Clark, G. W., 1965, Phys. Rev. Letters, 14, 91.

3. Giacconi, R., Gorenstein, P., Gursky, H., and Waters, J., 1967, Am. Sci. & Engr. Publ. No. ASE-1587.

4. McCracken, K. G., 1966, Science 154, 1000.

5. Grader, R. J., Hill, R. W., Seward, F. D., and Toor, A., 1966, Science 152, 1499.

6. Overbeck, J. W., Womack, E. A., and Tananbaum, H. D., 1967, Ap. J. 150, 47.

7. Chodil, G., Mark, H., Rodriguez, R., and Swift, C. D., 1968, Ap. J. 151, L1.

8. Evans, R., The Atomic Nucleus (McGraw-Hill, 1955).

9. Engelkemeir, D., 1956, Rev. Sci. Instr. 27, 589.

10. Axel, P., 1954, Rev. Sci. Instr. 25, 391.

11. Meyerhof, W. E., and West, H. I., 1954, Rev. Sci. Instr. 25, 1025.

12. Haymes, R. C., Ellis, D. V., Fishman, G. J., Glenn, S. W., and Kurfess, J. D., 1968, Ap. J. 151, L125.

13. Overbeck, J. W., and Tananbaum, H. D., 1968, Ap. J. 153, 899.

14. Bingham, R. G., and Clark, C. D., paper presented at November 1968 meeting of American Physical Society (to be published).

15. Rocchia, R., Rothenflug, R., Boclet, D., Durouchoux, Ph, (to be published in Phys. Rev. Letters).

16. Edwards, P. J., 1968 (to be published).

17. Byram, E. T., Chubb, T. A., and Friedman, H., 1966, Science 152, 66.

18. Kristian, J., Sandage, A. R., and Westphal, J., 1967, Ap. J. 150, L99.

19. Gorenstein, P., Kellogg, E. M., and Gursky, H., 1968, Am. Sci. & Engr. Publ. No. ASE-2105.

20. Bleeker, J. A. M., Burger, J. J., Deerenberg, A. J. M., Scheepmaker, A., Swanenburg, B. N., Tanaka, Y., Hayakawa, S., Makino, F., and Ogawa, H., 1968, Can. J. Phys. 46, S461.

21. Hudson, H. S., Primbsch, J. H., and Anderson, K. A., 1966, J. Geophys. Res. 71, 5665.

22. Seward, F., Chodil, G., Mark, H., Swift, C., and Toor, A., 1967, Ap. J., 150, 845.

23. Metzger, A. E., Anderson, E. C., Van Dilla, M. A., Arnold. J. R., 1964, Nature 264, 766.

24. Clark, G. W., Garmire, G., and Kraushaar, W. L. 1968, Ap. J. 153, L203.

25. Brini, D., Ciriegi, U., Fuligni, F., Gandolfi, A. and Moretti, E., 1965, Nuovo Cimento 38, 4710.

26. Jackson, J. D., Classical Electrodynamics (John Wiley & Sons, 1962), 470.

27. Schwinger, J., 1949, Phys. Rev. 75, 1912.

28. Corson, D. R., 1953, Phys. Rev. 90, 748.

29. Morrison, P., 1967, Ann. Rev. Astro. Astrophys. 5, 325.

30. Felton, J., and Morrison, P., 1966, Ap. J. 146, 686.

31. Allen, C. W., Astrophysical Quantities, (Athlone Press, 1963), 100.

32. Ney, E. P., and Stein, W. A., 1968, Ap. J. 152, L21.

33. Kardashev, N. S., 1962, Sov. Astro. 6, No. 3, 317 (Transl.).

34. Oda, Minoru, 1968, Space Sci. Rev. 8, 507.

35. Gorenstein, P., Giacconi, R., and Gursky, H., 1967, Ap. J. 150, L85.

36. Bowyer, C. S., Field, G. B., and Mack, J. E., 1968, Nature 217, 32.

37. Ables, J. G., 1968, Publ. No. ADP65, Univ. of Adelaide, S. Australia.

38. Gould, R. J., and Burbidge, G. R., 1963, Ap. J., 138, 969.

39. Silk, J., 1969, Nature 221, 347.

40. Brecher, K., and Morrison, P., 1967, Ap. J. 150, L61.

41. McLaughlin, D. B., Introduction to Astronomy, (Hughton Miffin, 1961).

42. Weiler and Bell, Beta- and Gamma-Ray Spectroscopy, edited by Kai Siegbahn, Interscience Publishers, Inc., New York, 1965.

43. Scarborough, J. B., Numerical Mathematical Analysis, Johns Hopkins Press, 1950.

44. The American Ephemeris, U. S. Government Printing Office, Washington, D. C. 1965.

45. Lewin, W.H.G., Clar, G. W. and Smith, W. B., 1968, Astrophys. J. 46, S409.

ACKNOWLEDGMENTS

I would like to express my deepest appreciation to Dr. W. R. Webber for his invaluable guidance and encouragement through this research.

For their assistance with the construction of the experiment and with the data analysis, I would like to thank Mr. Donald Kvist, Mr. John Droracek, Mr. Jeffrey Hammer, Mr. James Kish, Mr. Charles Gilman and Mr. Cordell Kittelson.

I am most grateful to Mrs. Iona Quesnell for the typing of this work.

Lastly, I would like to express my gratitude to my wife for her patience and encouragement over the period of this research.

This work has been supported by the National Aeronautics and Space Administration Grant No. NGL-24-005-008.

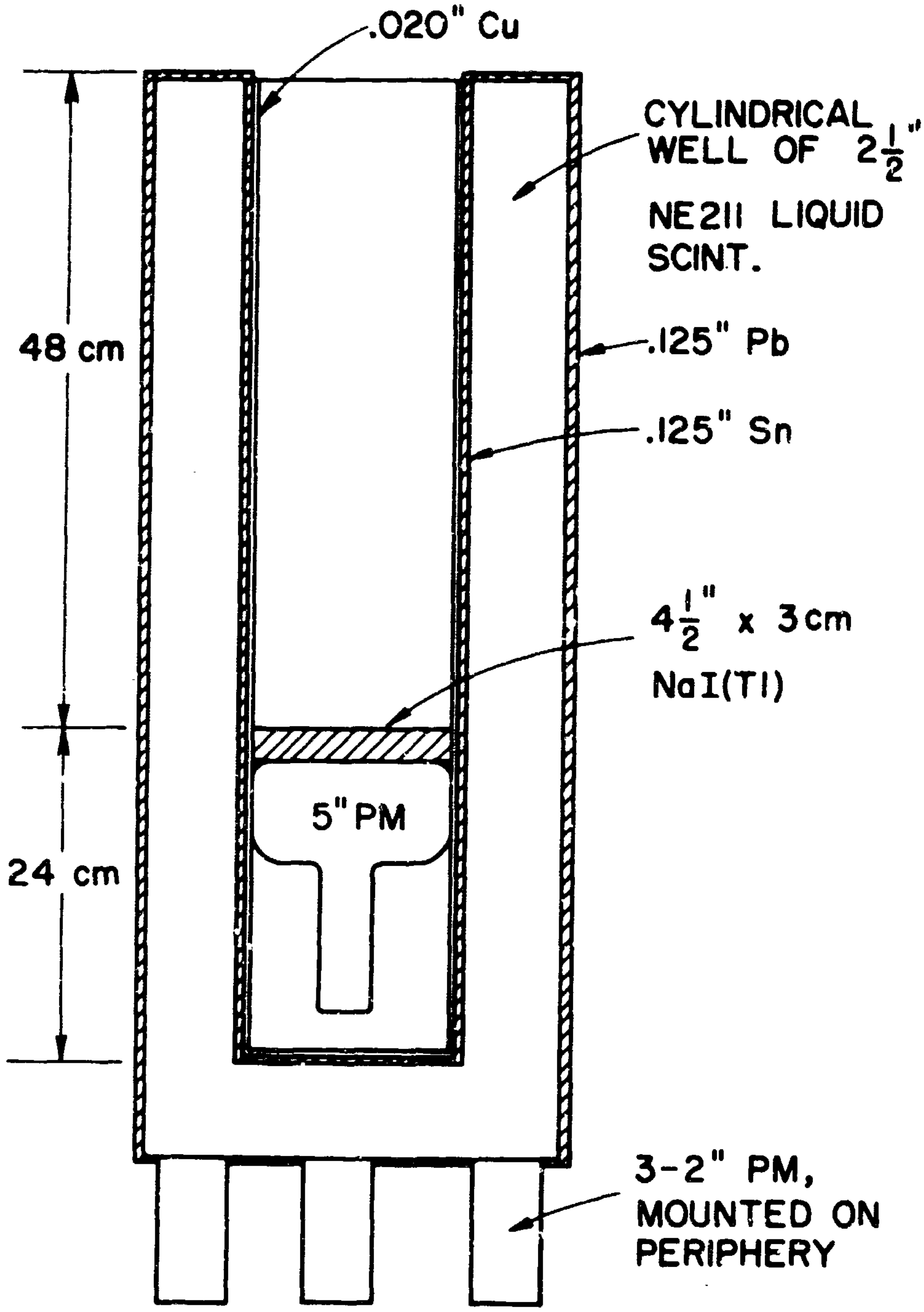
.020" Cu
CYLINDRICAL WELL OF 2 1/2"
NE211 LIQUID SCINT.
.125" Pb
.125" Sn
4 1/2" x 3cm
NaI(Tl)
48 cm
24 cm
5"PM
3-2" PM, MOUNTED ON PERIPHERY

Figure 1

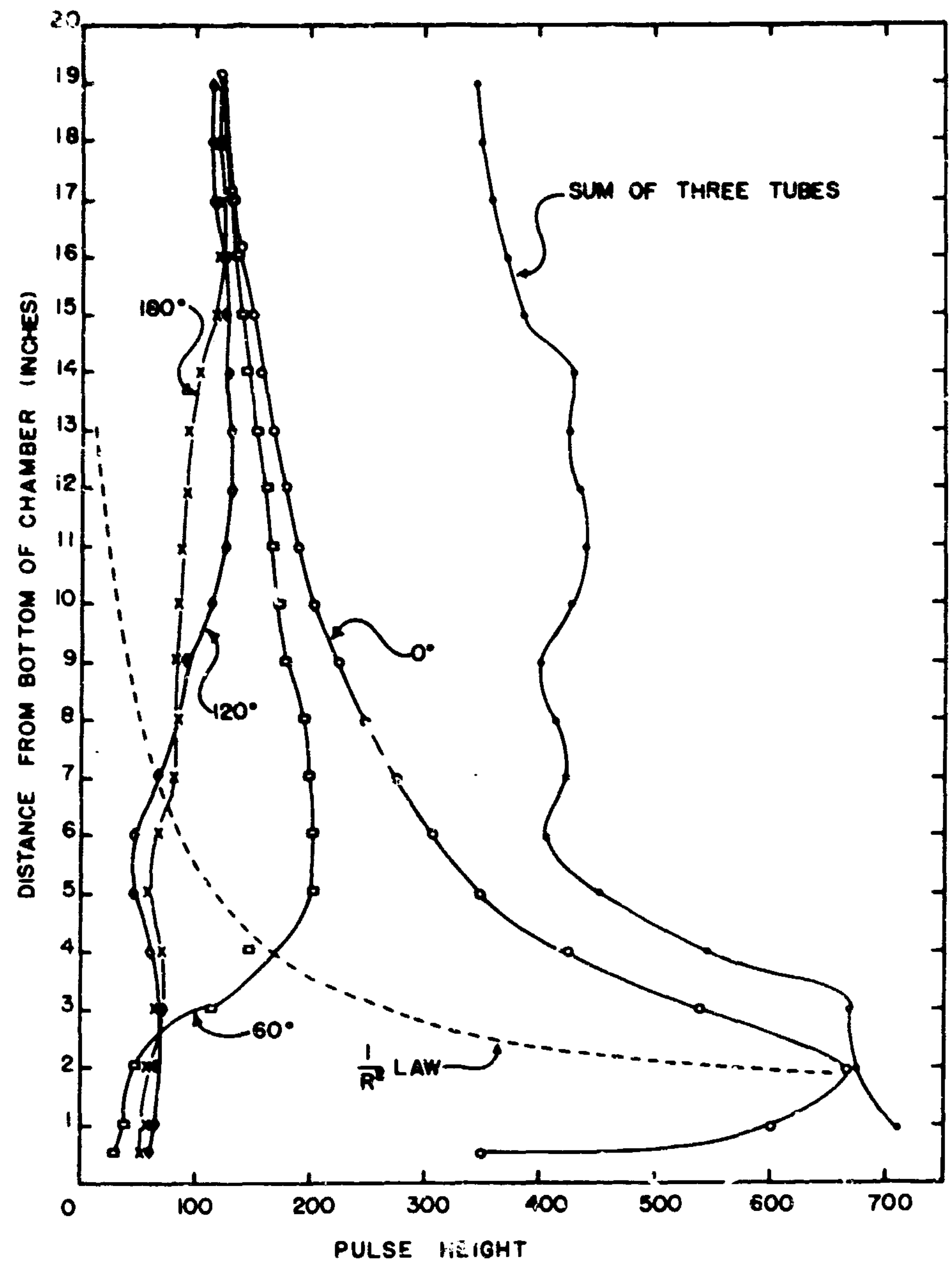

SUM OF THREE TUBES
180°
0°
120°
60°
$\frac{1}{R^2}$ LAW
DISTANCE FROM BOTTOM OF CHAMBER (INCHES)
PULSE HEIGHT
0
100
200
300
400
500
600
700
20
19
18
17
16
15
14
13
12
11
10
9
8
7
6
5
4
3
2
1

Figure 2

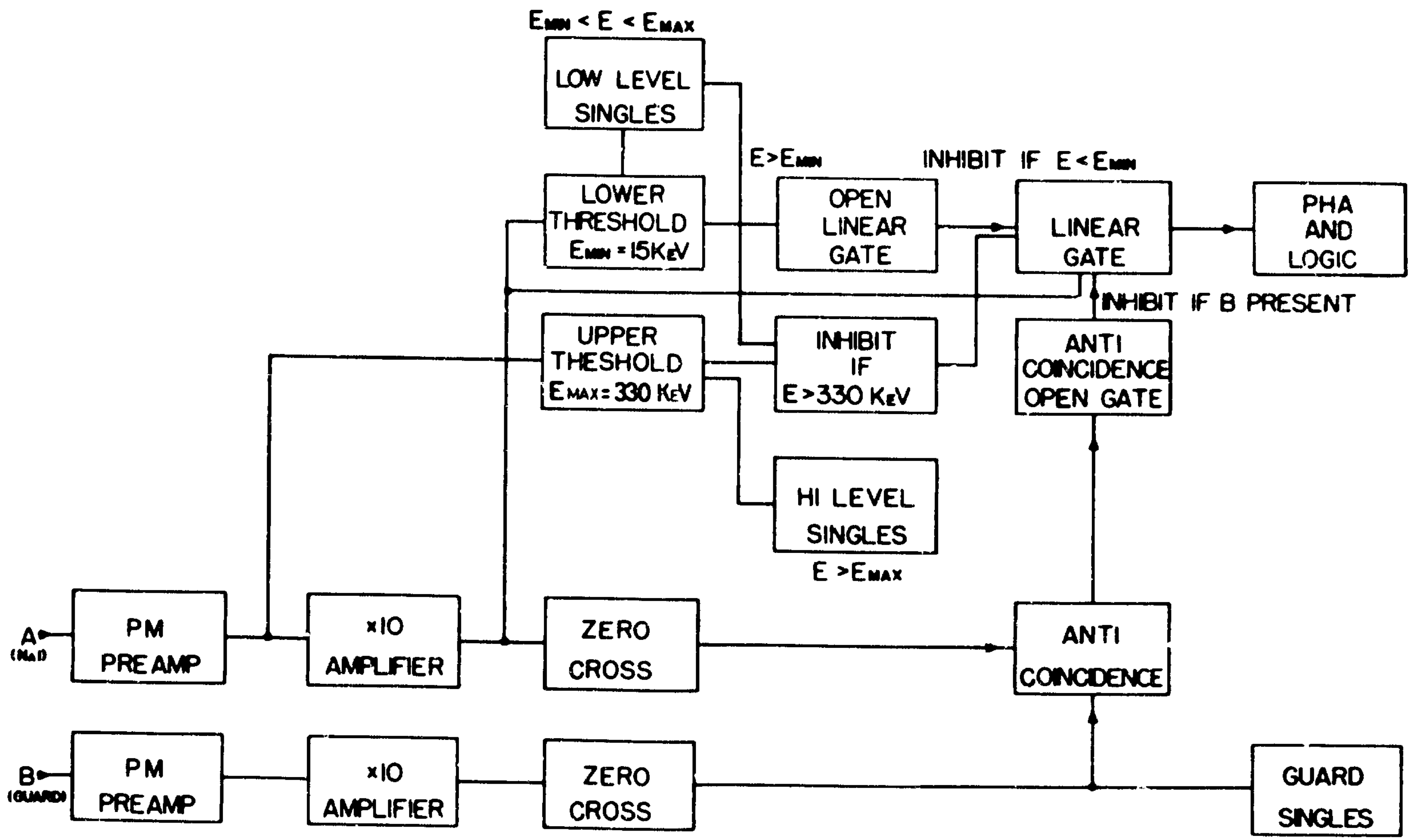
E MIN < E < E MAX
LOW LEVEL SINGLES
LOWER THRESHOLD E MIN = 15 KeV
E > E MIN
OPEN LINEAR GATE
INHIBIT IF E < E MIN
LINEAR GATE
PHA AND LOGIC
INHIBIT IF B PRESENT
UPPER THESHOLD E MAX = 330 KeV
INHIBIT IF E > 330 KeV
ANTI COINCIDENCE OPEN GATE
HI LEVEL SINGLES
E > E MAX
A (NaI)
PM PREAMP
x10 AMPLIFIER
ZERO CROSS
ANTI COINCIDENCE
B (GUARD)
PM PREAMP
x10 AMPLIFIER
ZERO CROSS
GUARD SINGLES

Figure 3

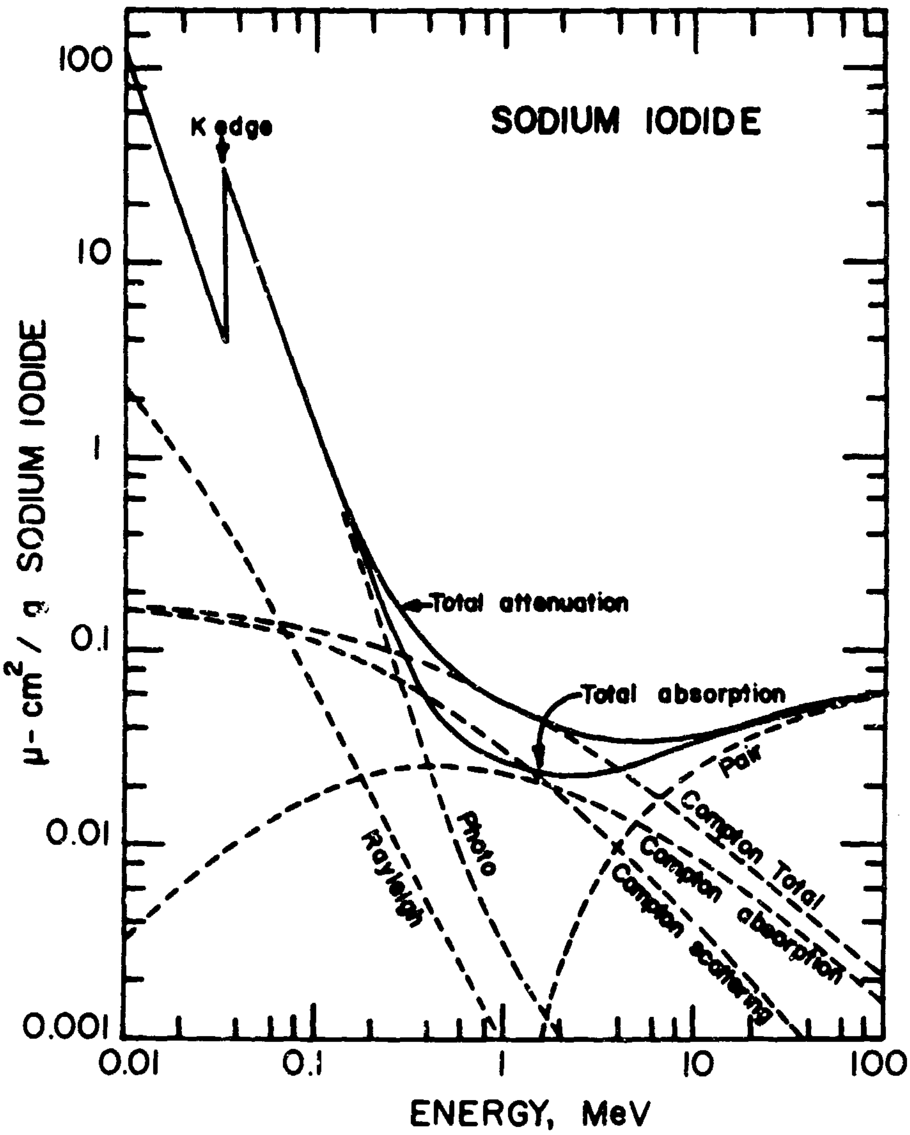
SODIUM IODIDE
K edge
Total attenuation
Total absorption
Pair
Compton Total
Compton absorption
Compton scattering
Photo
Rayleigh
100
10
1
0.1
0.01
0.001
0.01
0.1
1
10
100
ENERGY, MeV
μ- cm² / g SODIUM IODIDE

Figure 4

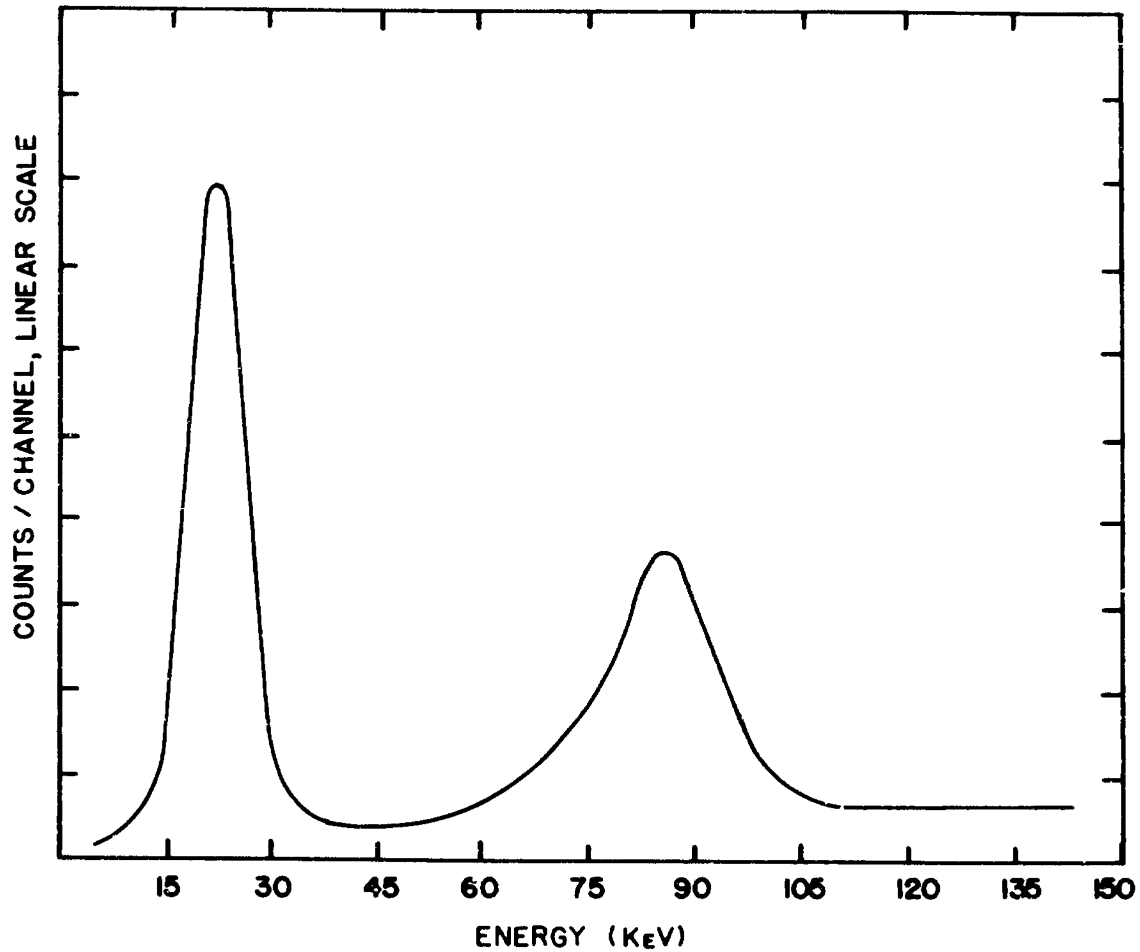

COUNTS / CHANNEL, LINEAR SCALE
15
30
45
60
75
90
105
120
135
150
ENERGY (KeV)

Figure 5

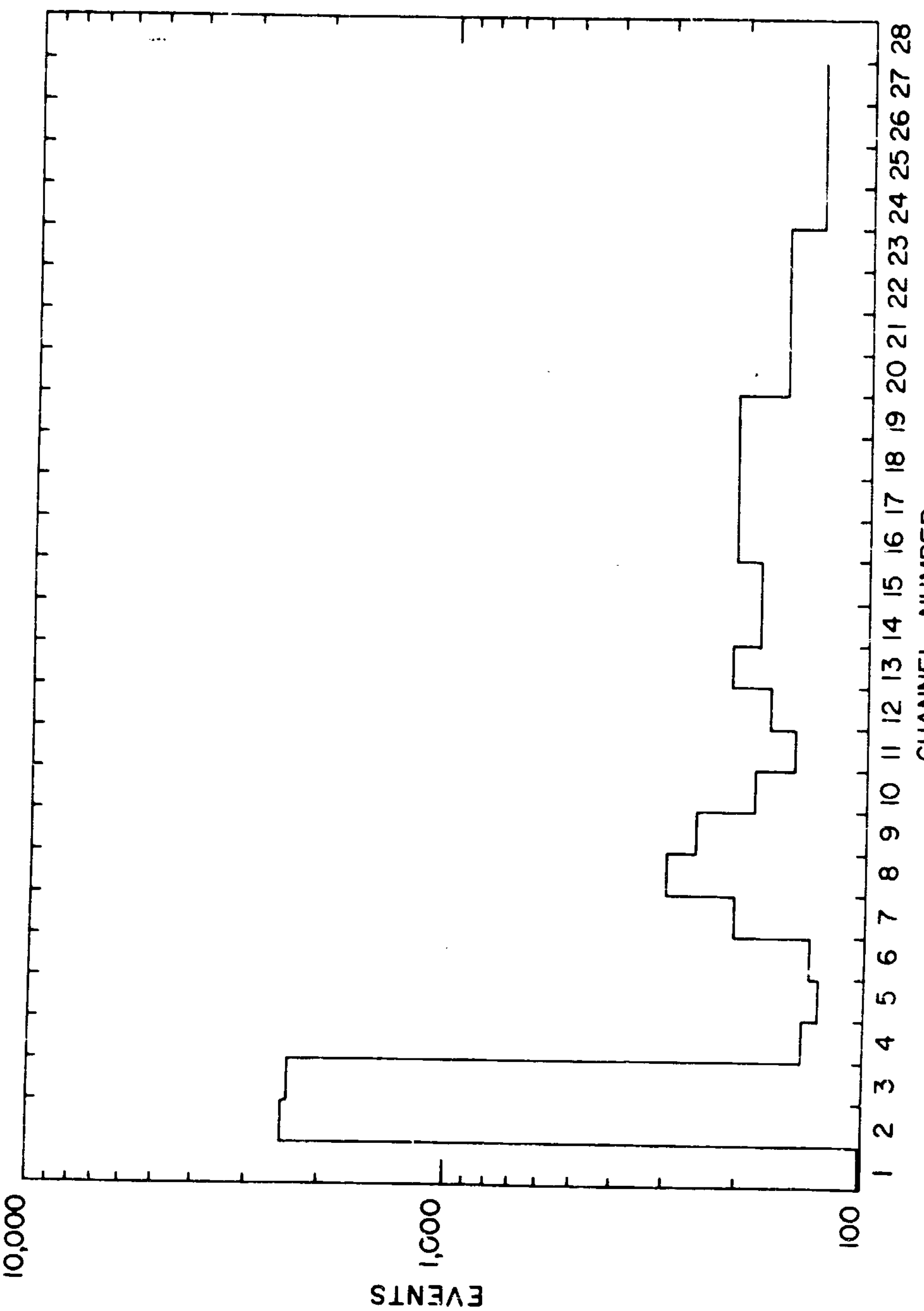
10,000
1,000
100
EVENTS
1 2 3 4 5 6 7 8 9 10 11 12 13 14 15 16 17 18 19 20 21 22 23 24 25 26 27 28
CHANNEL NUMBER

Figure 6

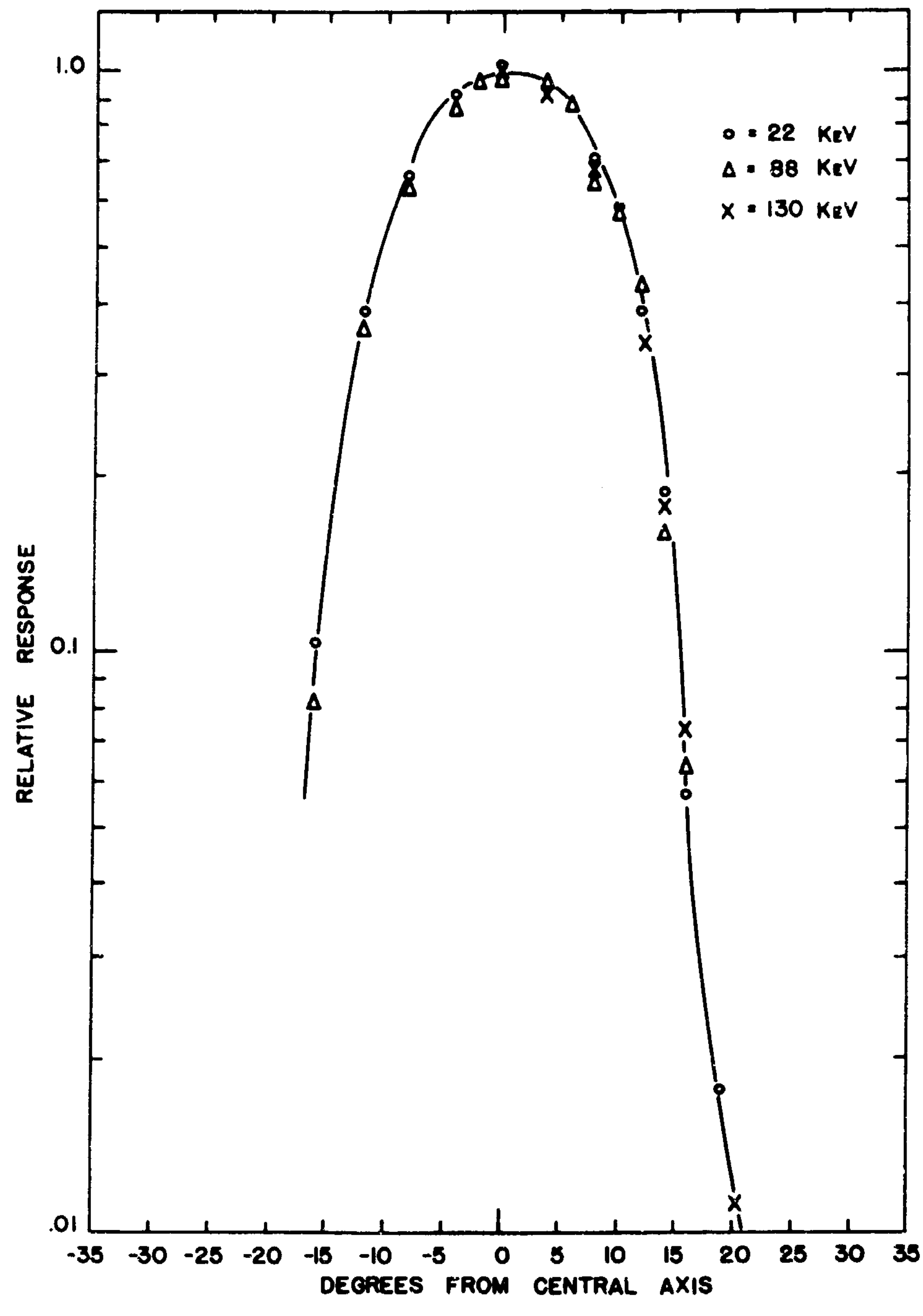

1.0
0.1
.01
RELATIVE RESPONSE
o = 22 KeV
Δ = 88 KeV
X = 130 KeV
-35 -30 -25 -20 -15 -10 -5 0 5 10 15 20 25 30 35
DEGREES FROM CENTRAL AXIS

Figure 7

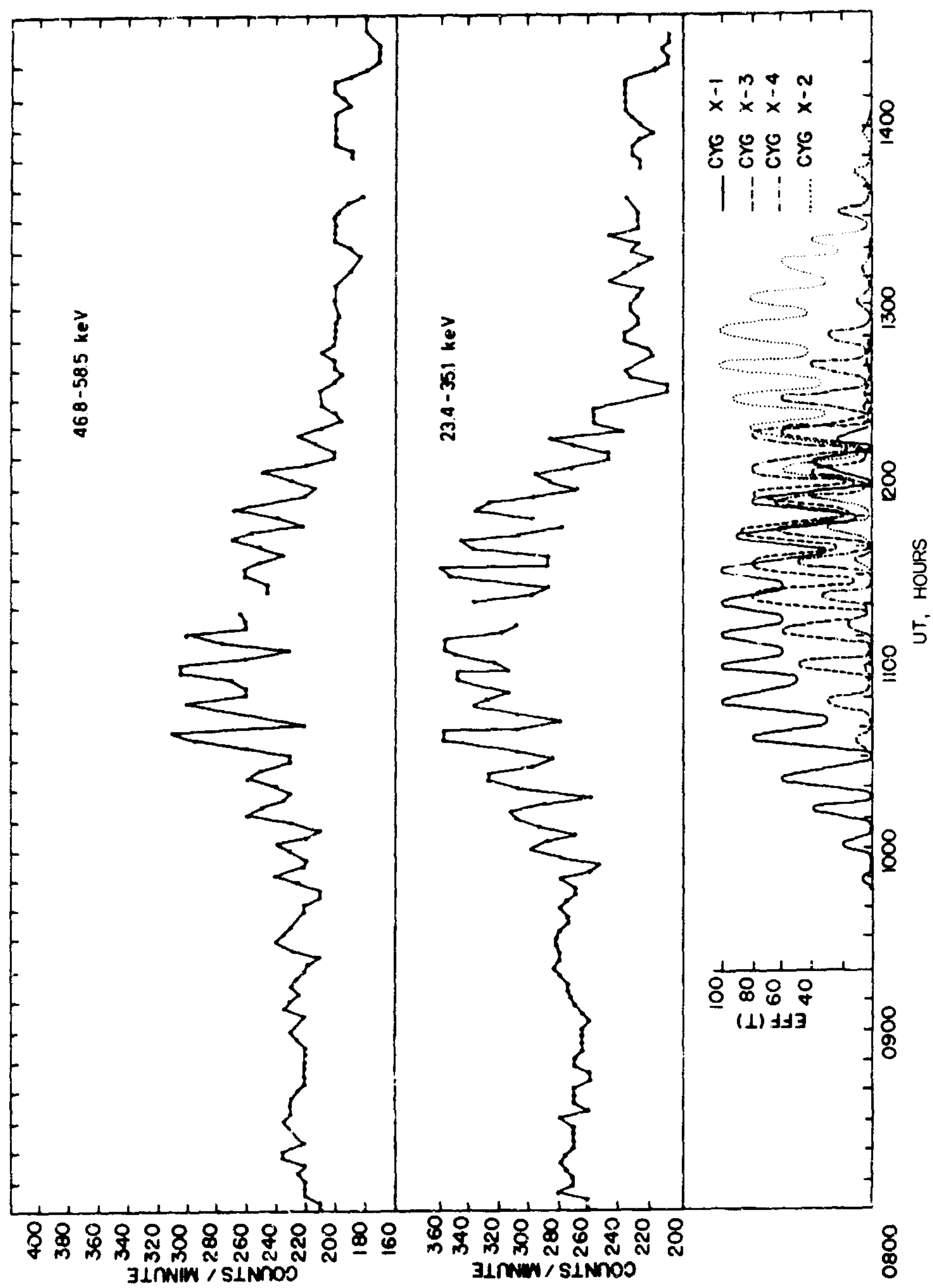
468-585 keV
23.4-351 keV
COUNTS / MINUTE
COUNTS / MINUTE
EFF (T)
UT, HOURS
CYG X-1
CYG X-3
CYG X-4
CYG X-2
0800
0900
1000
1100
1200
1300
1400

Figure 8

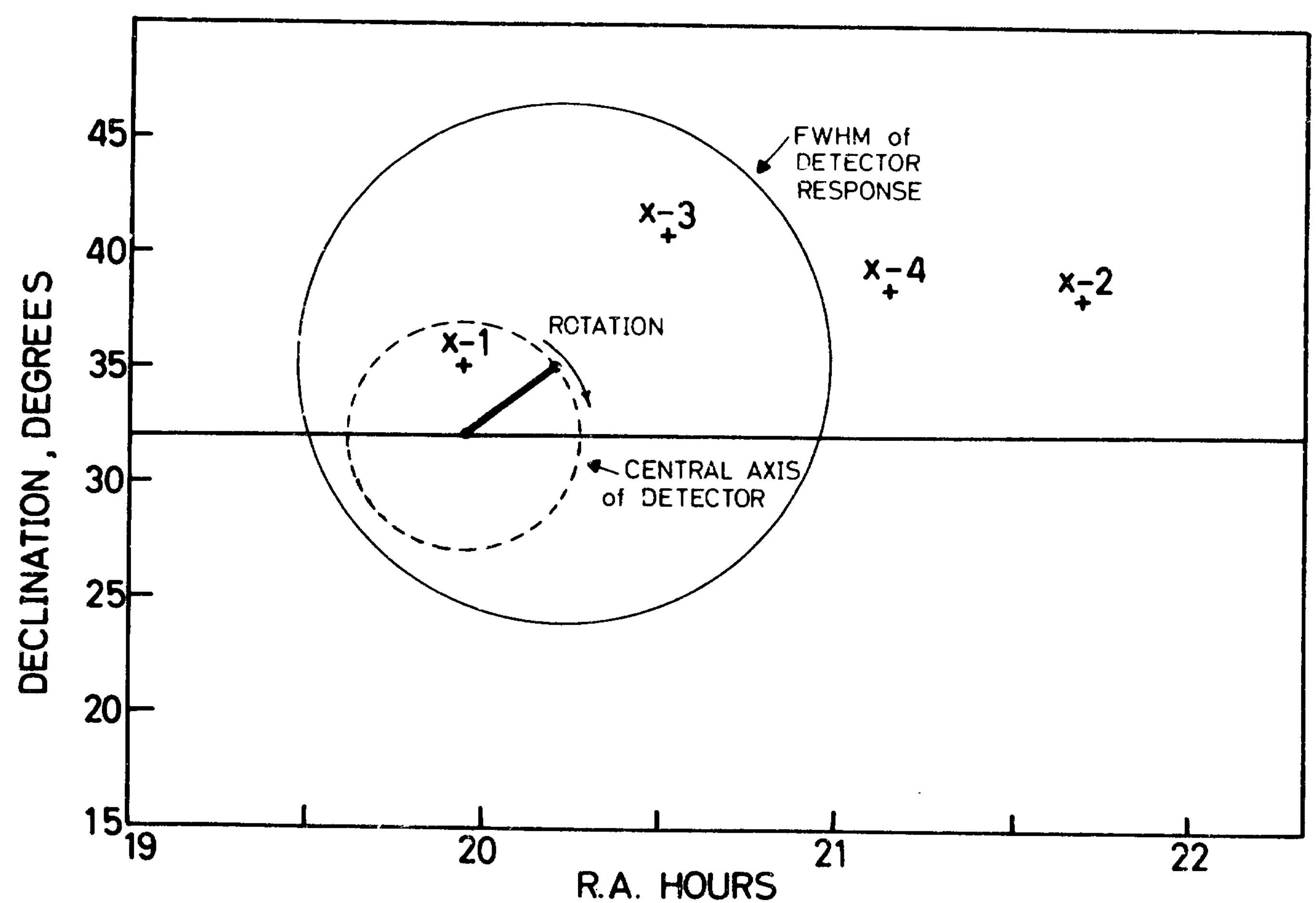

FWHM of
DETECTOR
RESPONSE
x-3
x-4
x-2
x-1
ROTATION
CENTRAL AXIS
of DETECTOR
45
40
35
30
25
20
15
19
20
21
22
DECLINATION, DEGREES
R.A. HOURS

Figure 9

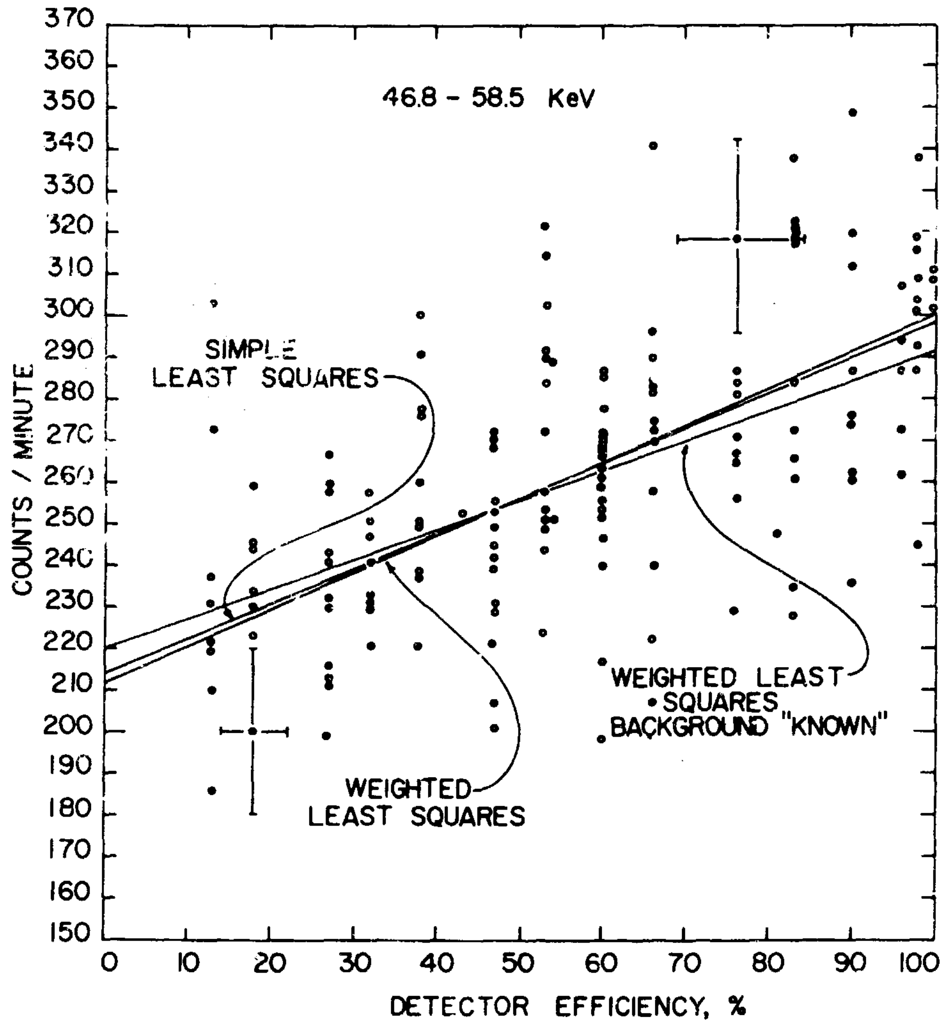
46.8 - 58.5 KeV
SIMPLE LEAST SQUARES
WEIGHTED LEAST SQUARES
WEIGHTED LEAST SQUARES BACKGROUND "KNOWN"
COUNTS / MINUTE
DETECTOR EFFICIENCY, %
370
360
350
340
330
320
310
300
290
280
270
260
250
240
230
220
210
200
190
180
170
160
150
0
10
20
30
40
50
60
70
80
90
100

Figure 10

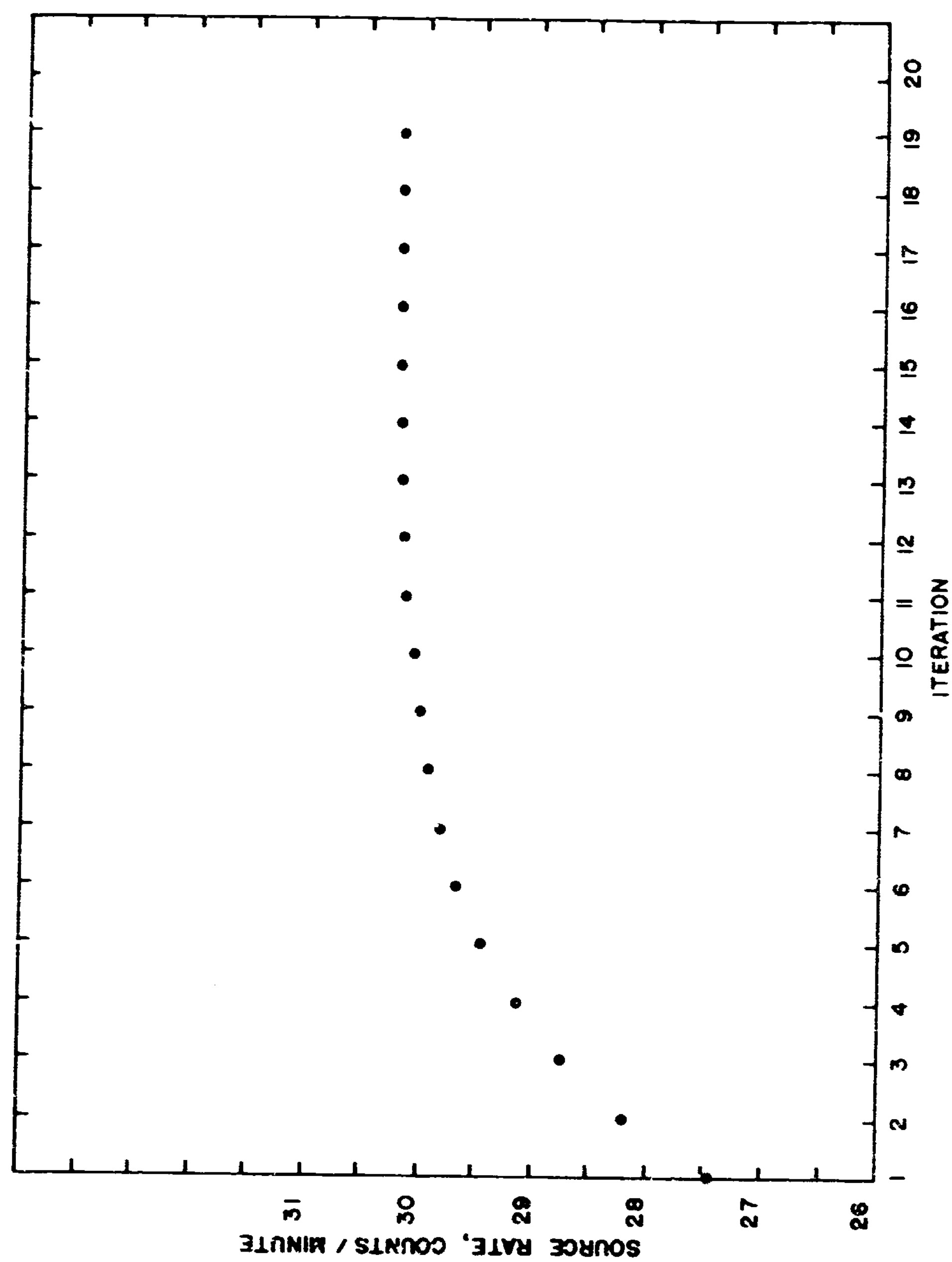
ITERATION
1 2 3 4 5 6 7 8 9 10 11 12 13 14 15 16 17 18 19 20
SOURCE RATE, COUNTS / MINUTE
26 27 28 29 30 31

Figure 11

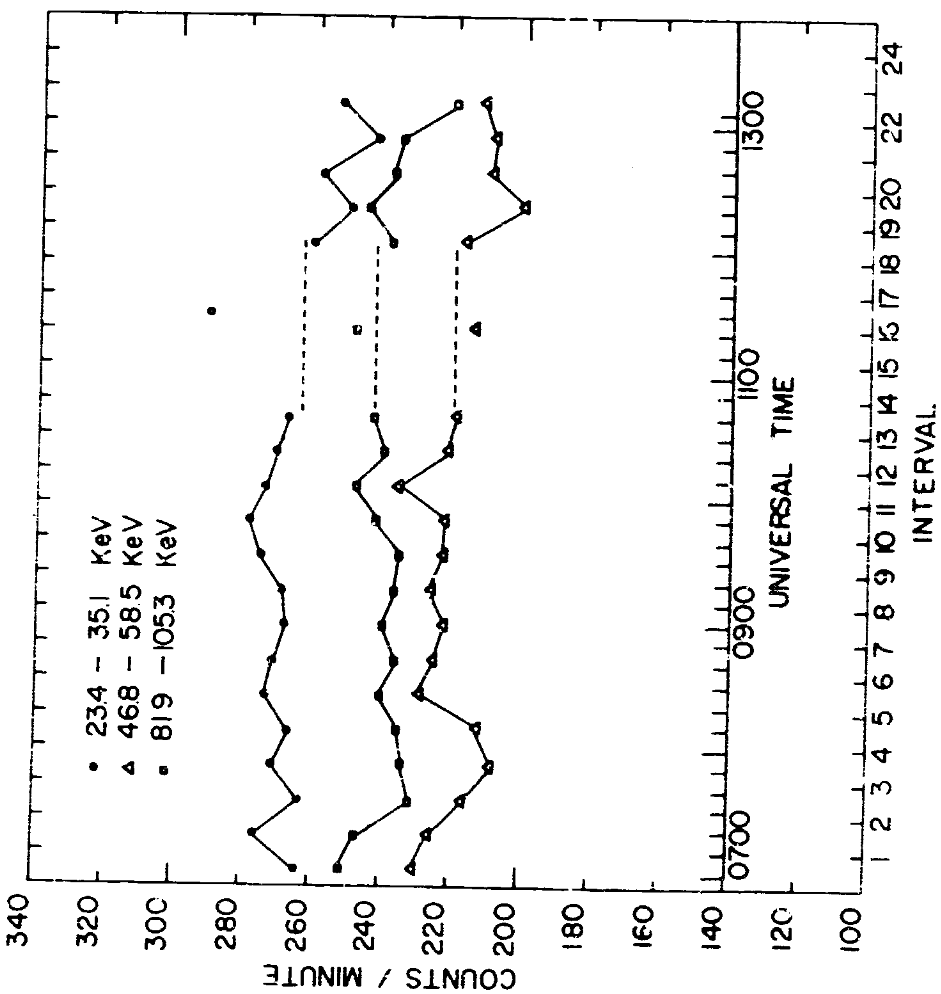

23.4 - 35.1 KeV
46.8 - 58.5 KeV
81.9 - 105.3 KeV
COUNTS / MINUTE
UNIVERSAL TIME
INTERVAL
0700
0900
1100
1300

Figure 12

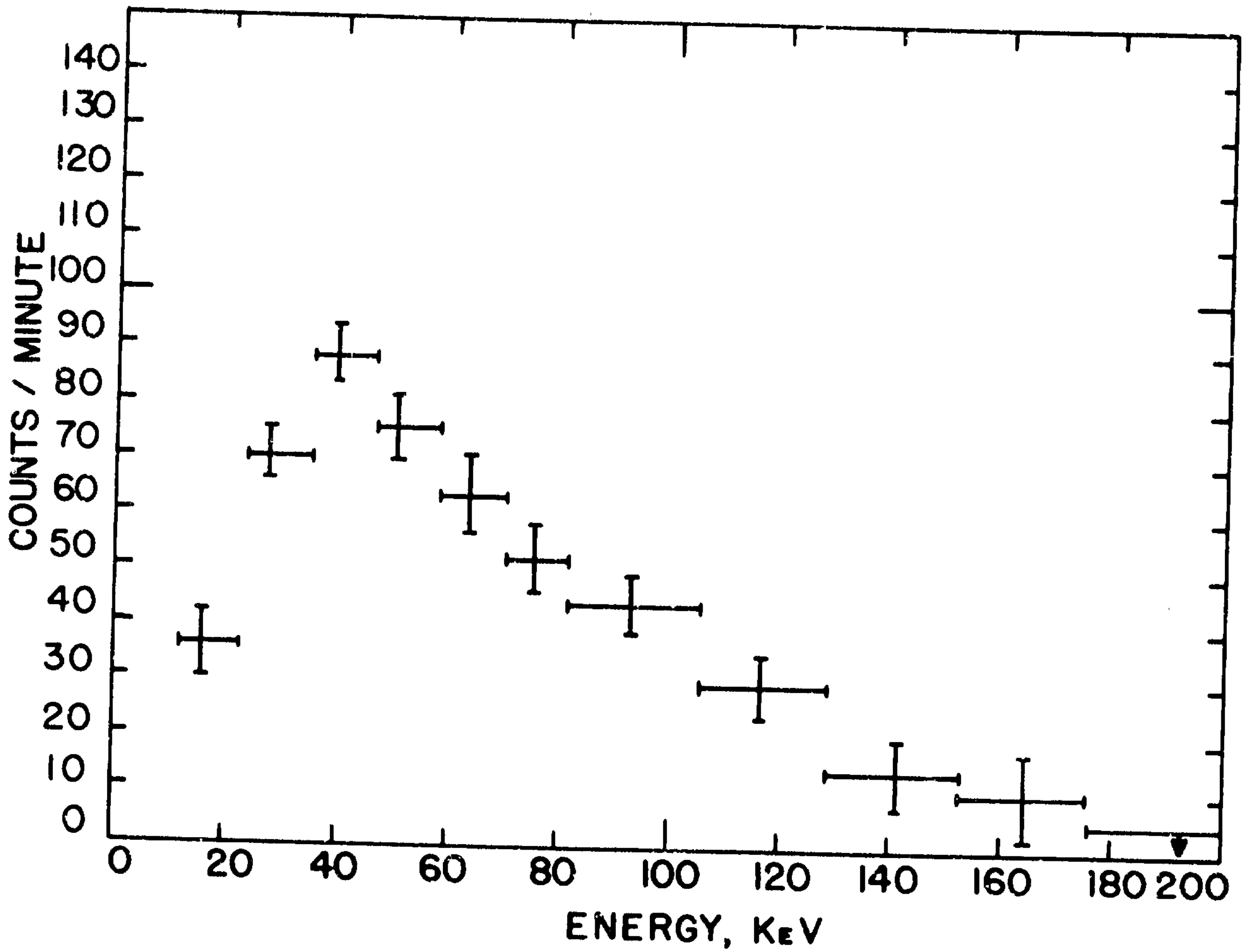
COUNTS / MINUTE
140
130
120
110
100
90
80
70
60
50
40
30
20
10
0
0
20
40
60
80
100
120
140
160
180
200
ENERGY, KeV

Figure 13

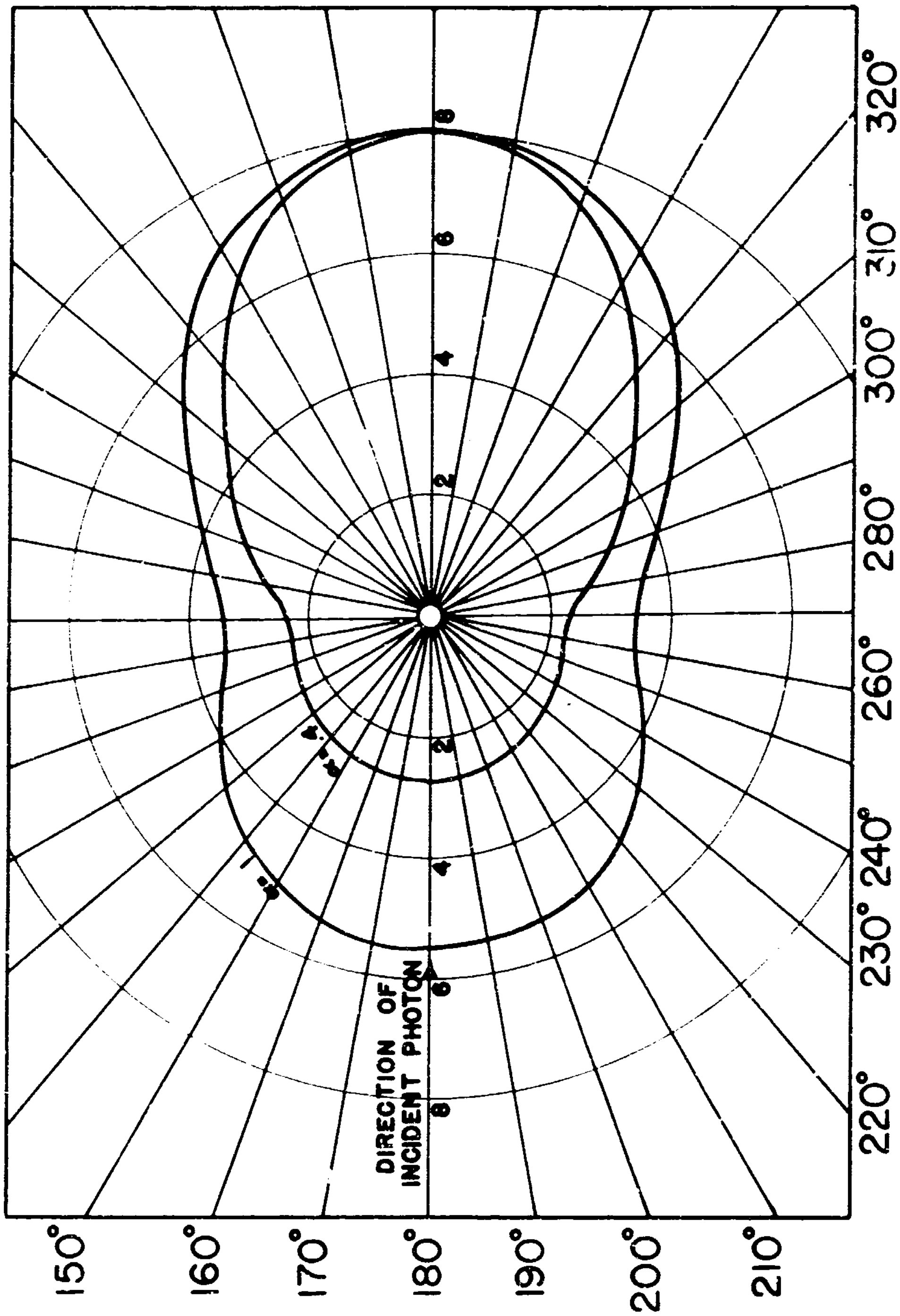

150°
160°
170°
180°
190°
200°
210°
220°
230°
240°
260°
280°
300°
310°
320°
DIRECTION OF
INCIDENT PHOTON
2
4
6
8

Figure 14

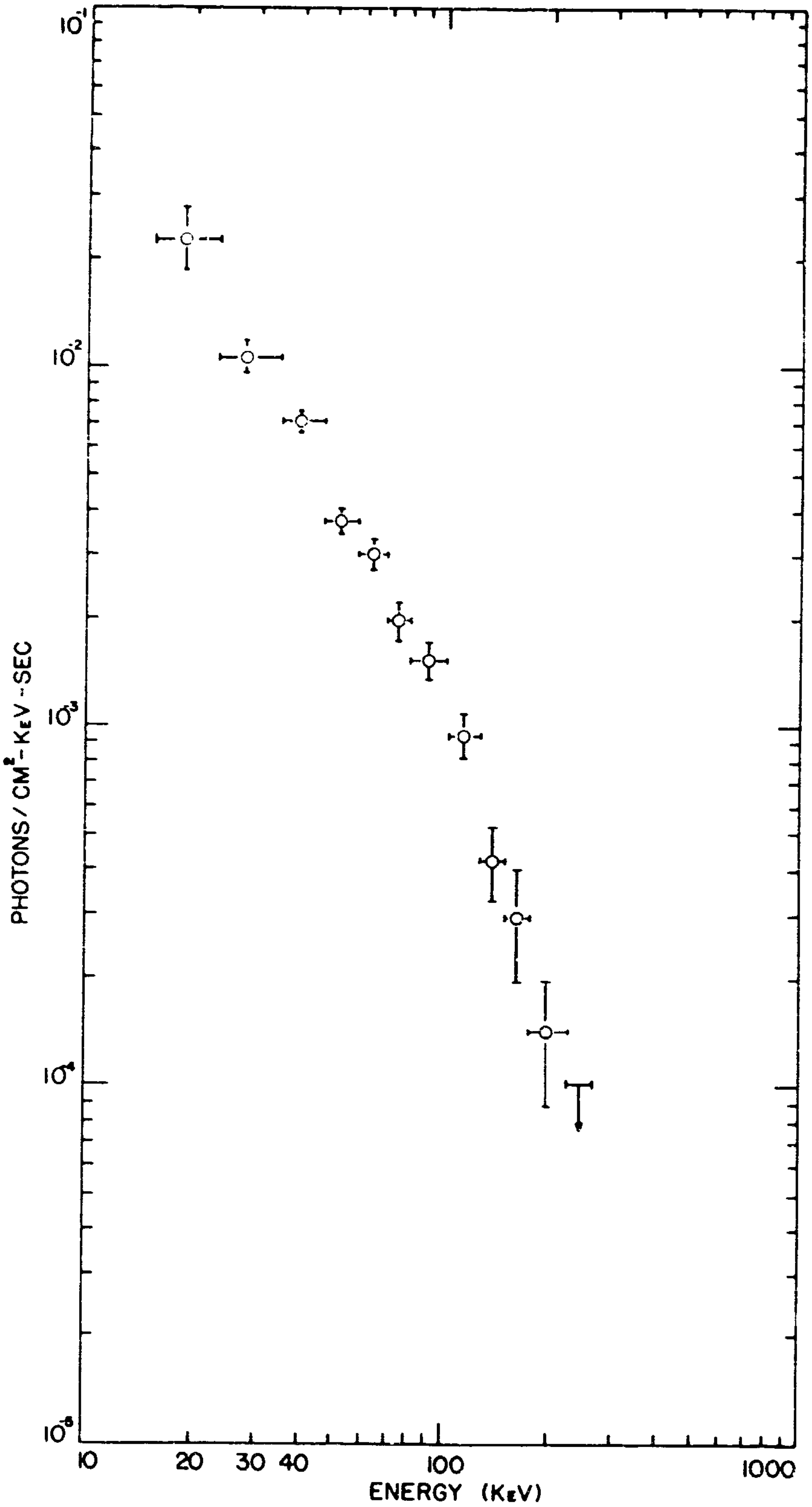

10⁻¹
10⁻²
10⁻³
10⁻⁴
10⁻⁵
PHOTONS/CM²-KeV-SEC
10
20
30
40
100
1000
ENERGY (KeV)

Figure 15

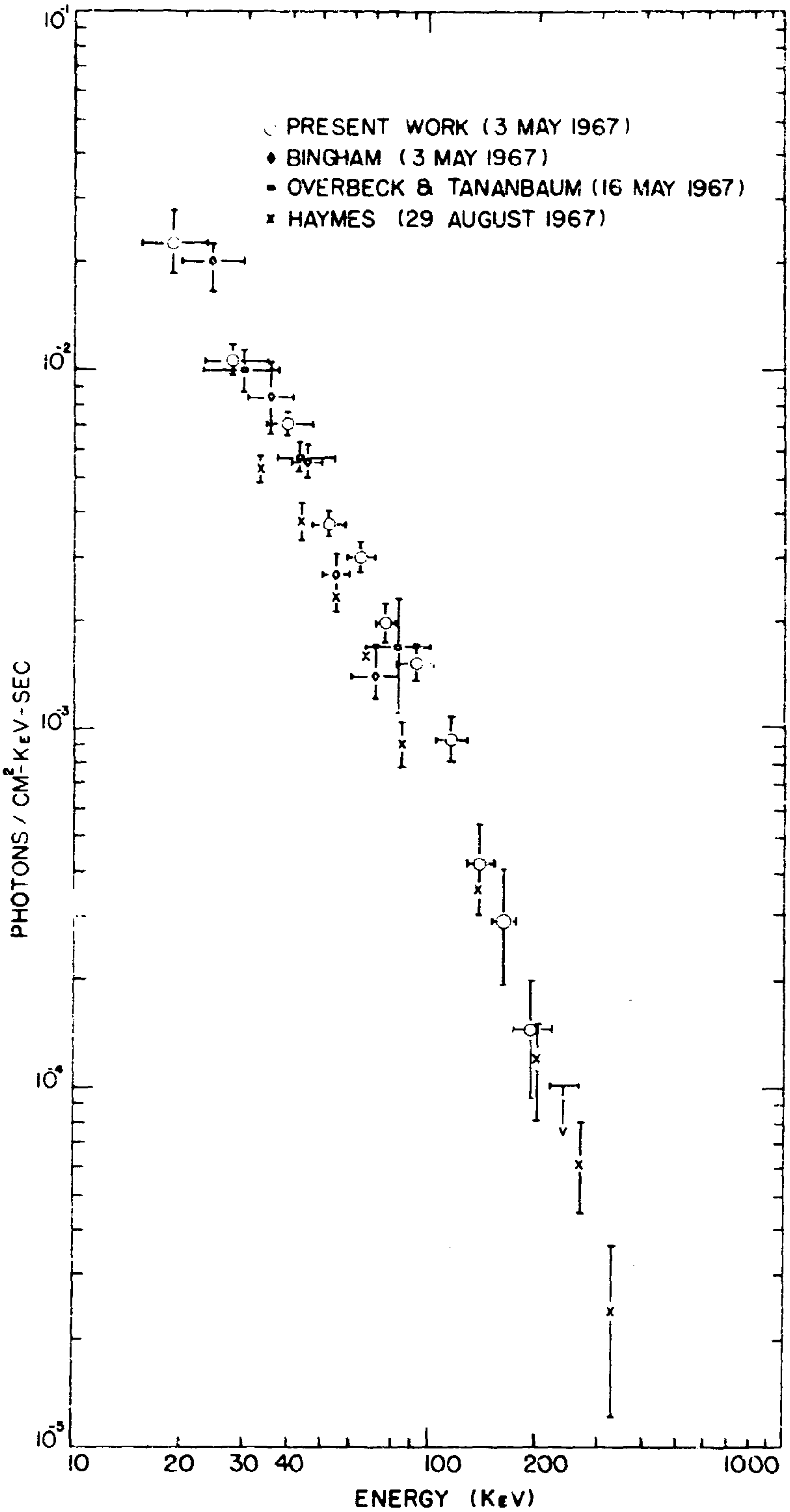
PRESENT WORK (3 MAY 1967)
BINGHAM (3 MAY 1967)
OVERBECK & TANANBAUM (16 MAY 1967)
HAYMES (29 AUGUST 1967)
10^{-1}
10^{-2}
10^{-3}
10^{-4}
10^{-5}
PHOTONS / CM^2-KeV-SEC
10
20
30
40
100
200
1000
ENERGY (KeV)

Figure 16

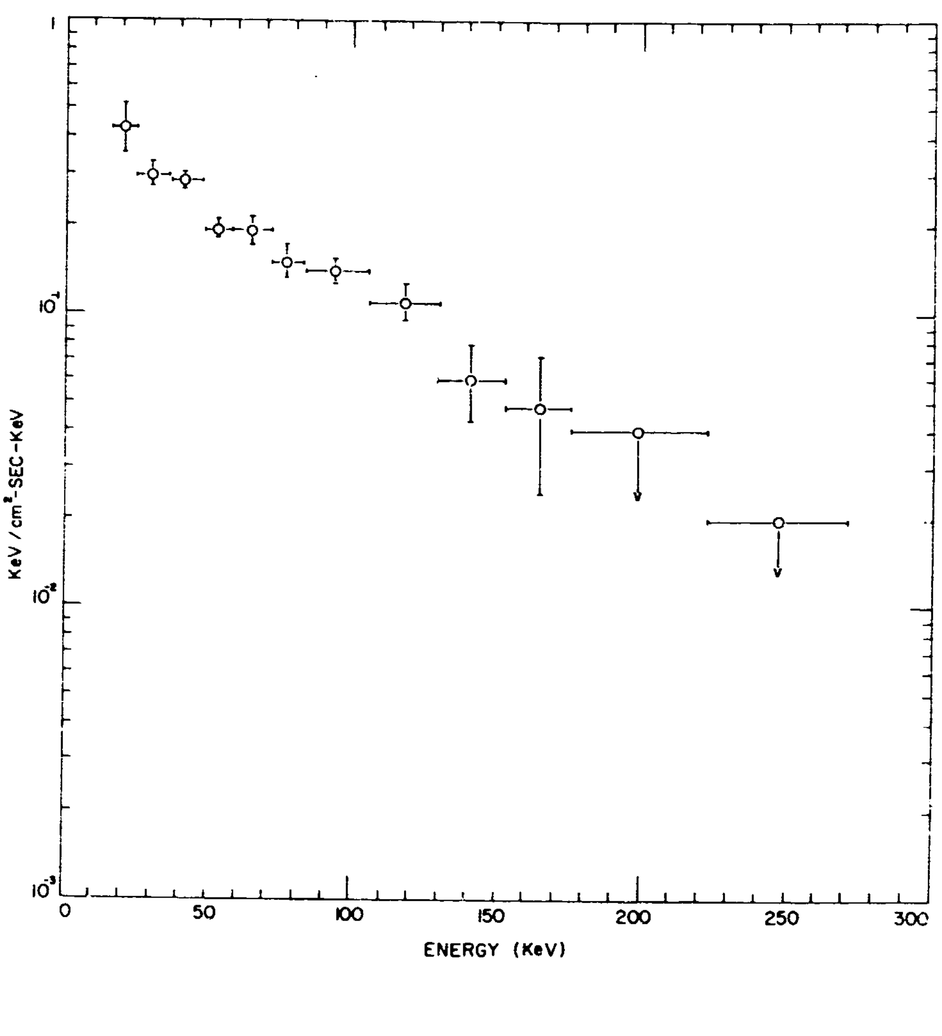

Figure 17a

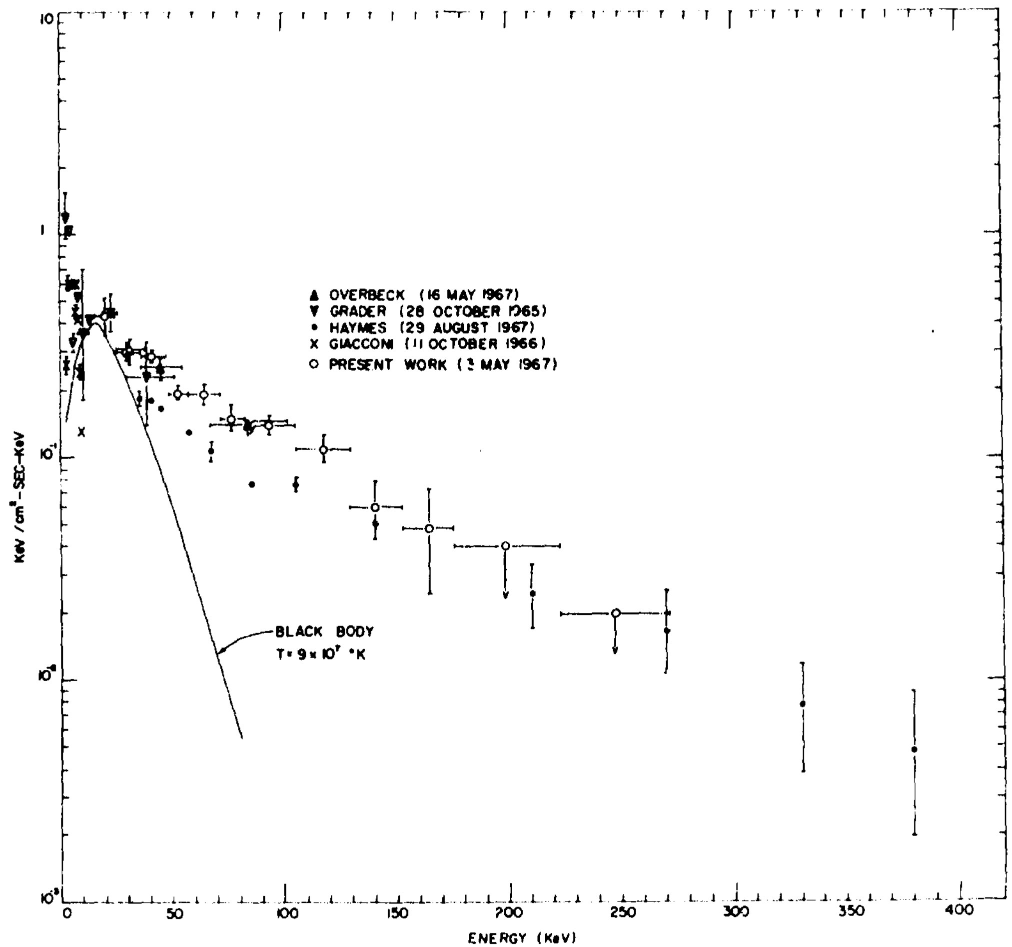
▲ OVERBECK (16 MAY 1967)
▼ GRADER (28 OCTOBER 1965)
• HAYMES (29 AUGUST 1967)
X GIACCONI (11 OCTOBER 1966)
O PRESENT WORK (3 MAY 1967)
BLACK BODY
T = 9 x 10^7 °K
KeV / cm^2 - SEC - KeV
10
1
10^-1
10^-2
10^-3
0
50
100
150
200
250
300
350
400
ENERGY (KeV)

Figure 17b

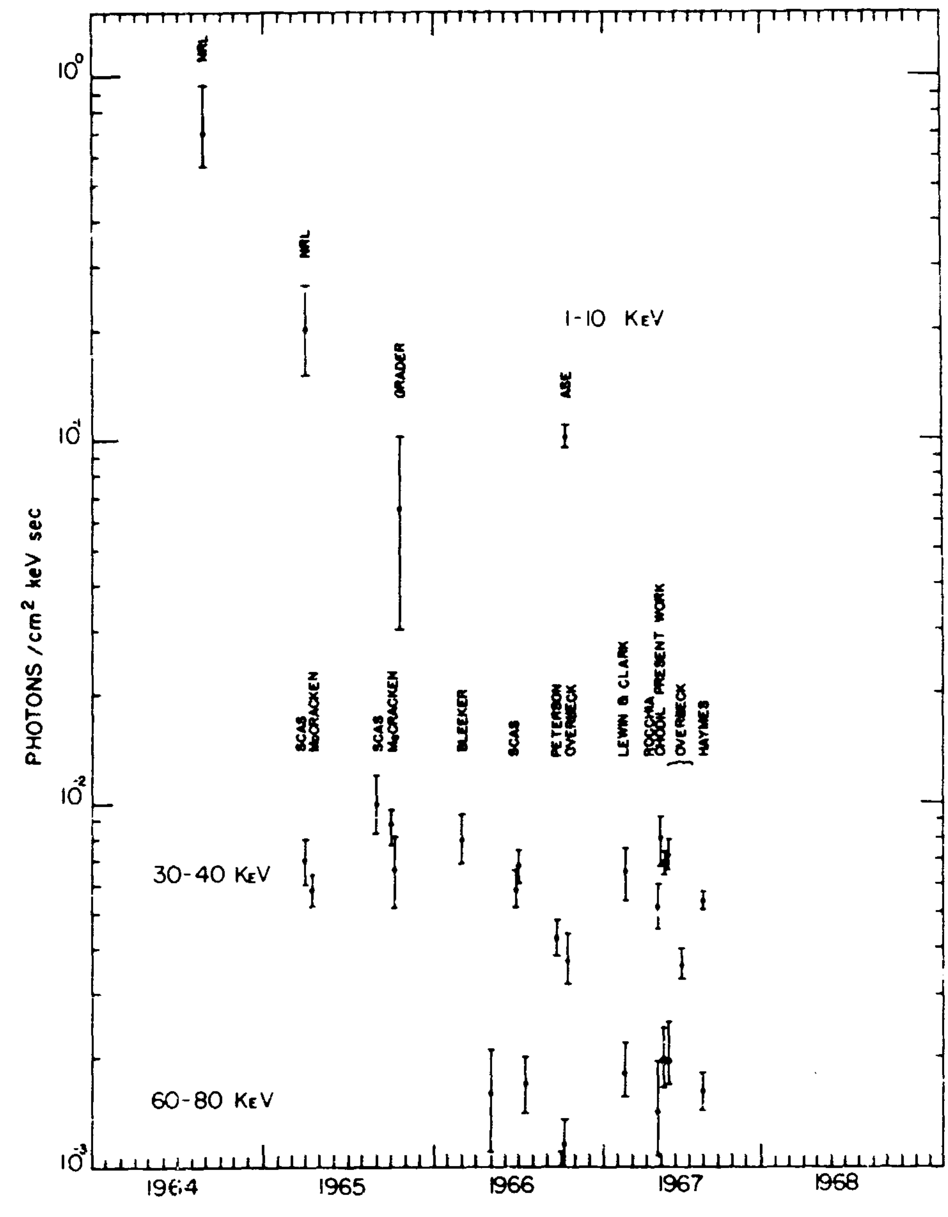
PHOTONS /cm² keV sec
10⁰
10⁻¹
10⁻²
10⁻³
1964
1965
1966
1967
1968
NRL
NRL
1-10 KeV
GRADER
ASE
SCAS McCRACKEN
SCAS McCRACKEN
BLEEKER
SCAS
PETERSON OVERBECK
LEWIN & CLARK
ROCCHIA
PRESENT WORK
OVERBECK
HAYMES
30-40 KeV
60-80 KeV

Figure 18

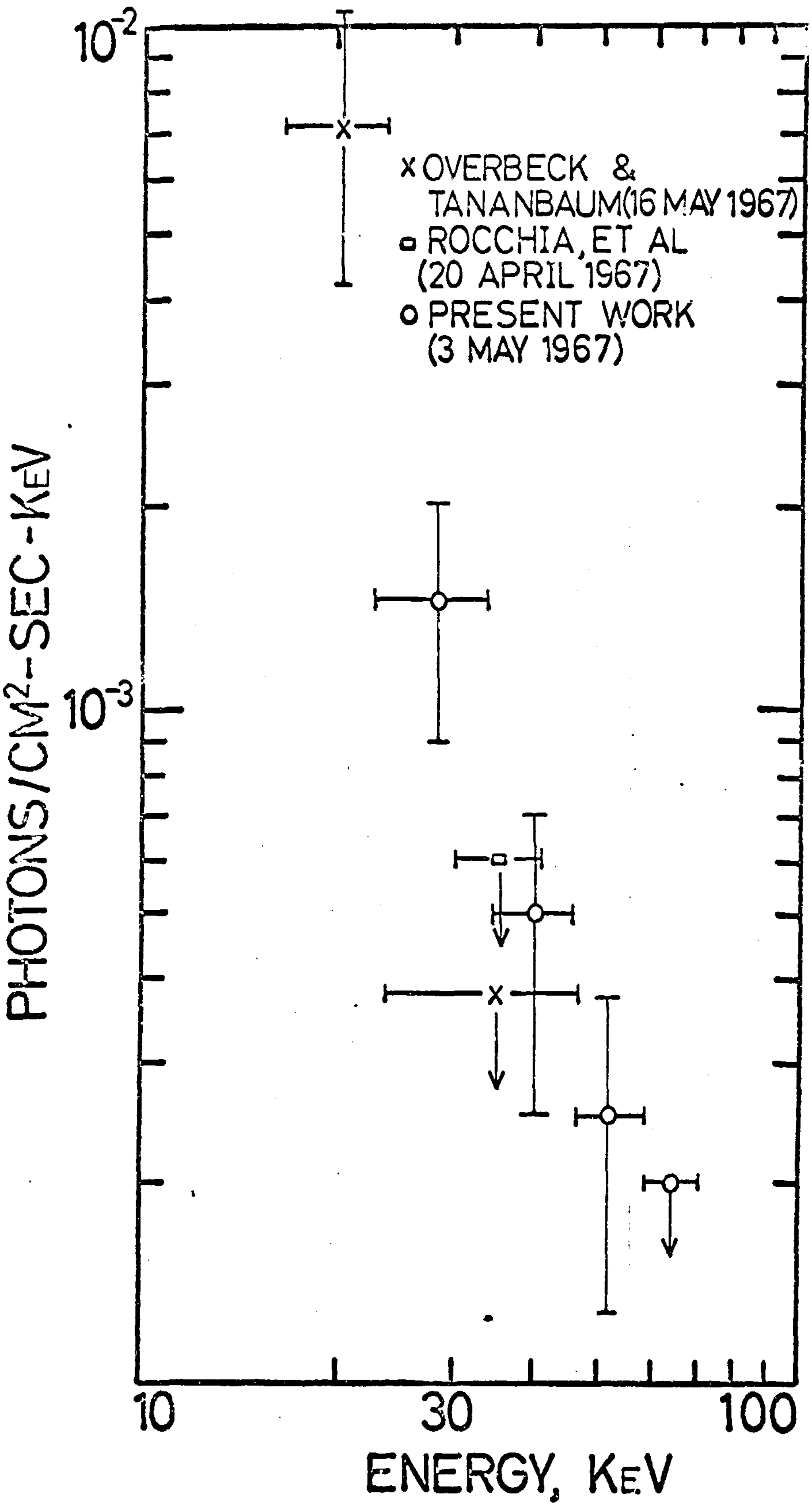
10^-2
10^-3
× OVERBECK &
TANANBAUM(16 MAY 1967)
▫ ROCCHIA, ET AL
(20 APRIL 1967)
o PRESENT WORK
(3 MAY 1967)
PHOTONS/CM²-SEC-KEV
10
30
100
ENERGY, KEV

FIGURE 19

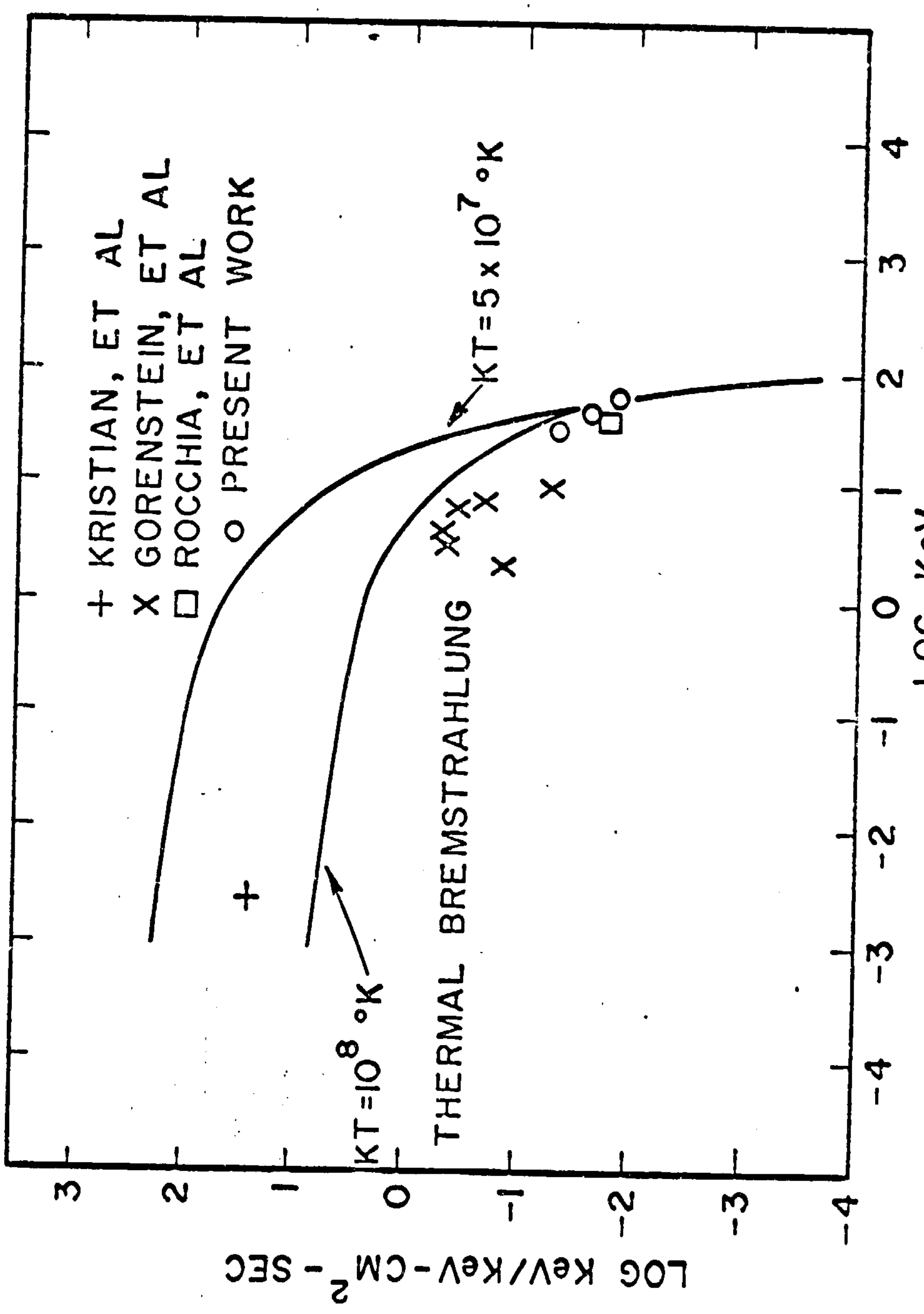
+ KRISTIAN, ET AL
X GORENSTEIN, ET AL
□ ROCCHIA, ET AL
o PRESENT WORK
KT=5 x 10^7 °K
KT=10^8 °K
THERMAL BREMSTRAHLUNG
LOG KeV
LOG KeV/KeV-CM^2 - SEC
-4
-3
-2
-1
0
1
2
3
4

FIGURE 20

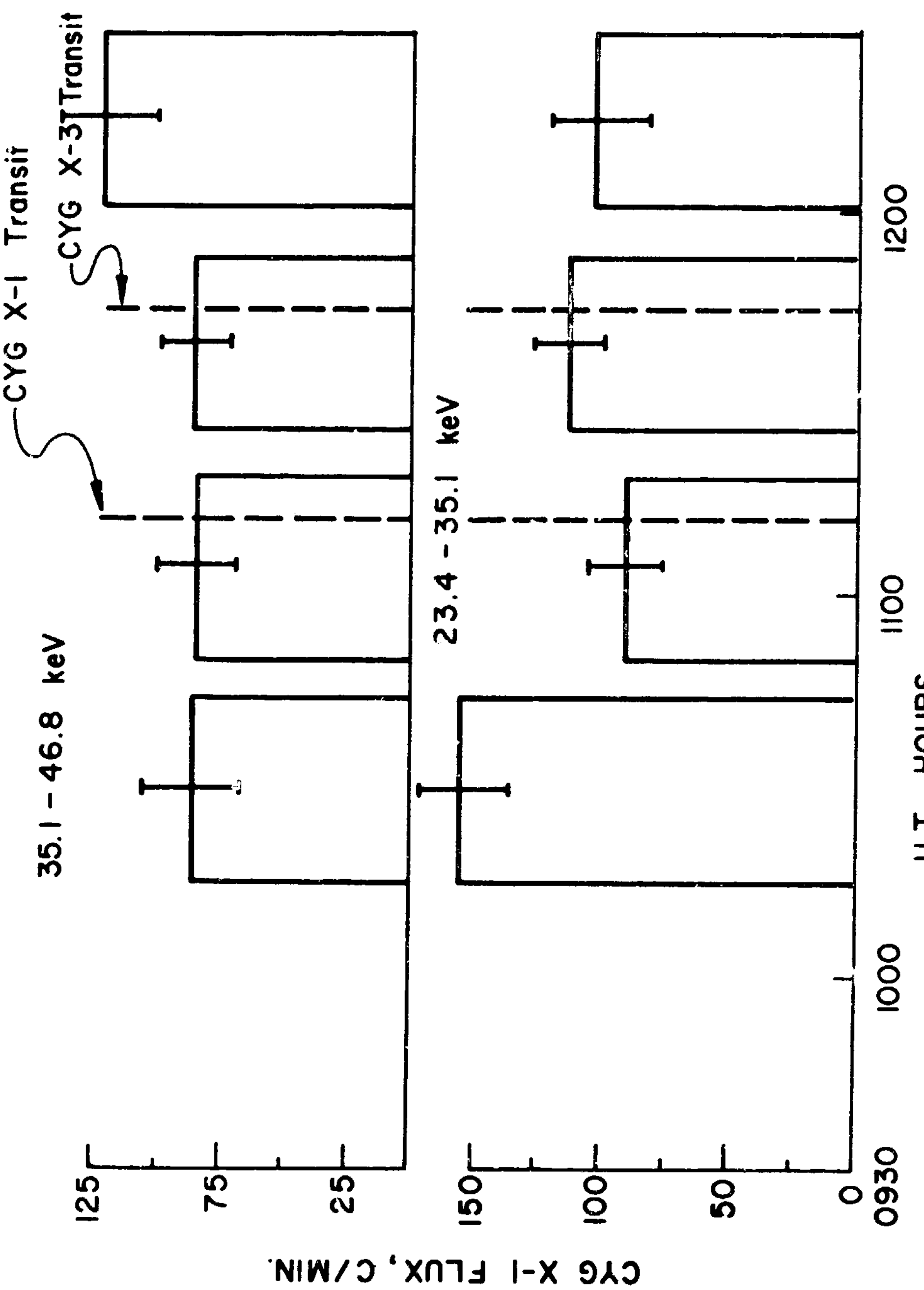
CYG X-I Transit
CYG X-3 Transit
35.1 - 46.8 keV
23.4 - 35.1 keV
125
75
25
150
100
50
0
0930
1000
1100
1200
U.T., HOURS
CYG X-I FLUX, C/MIN.

Figure 21

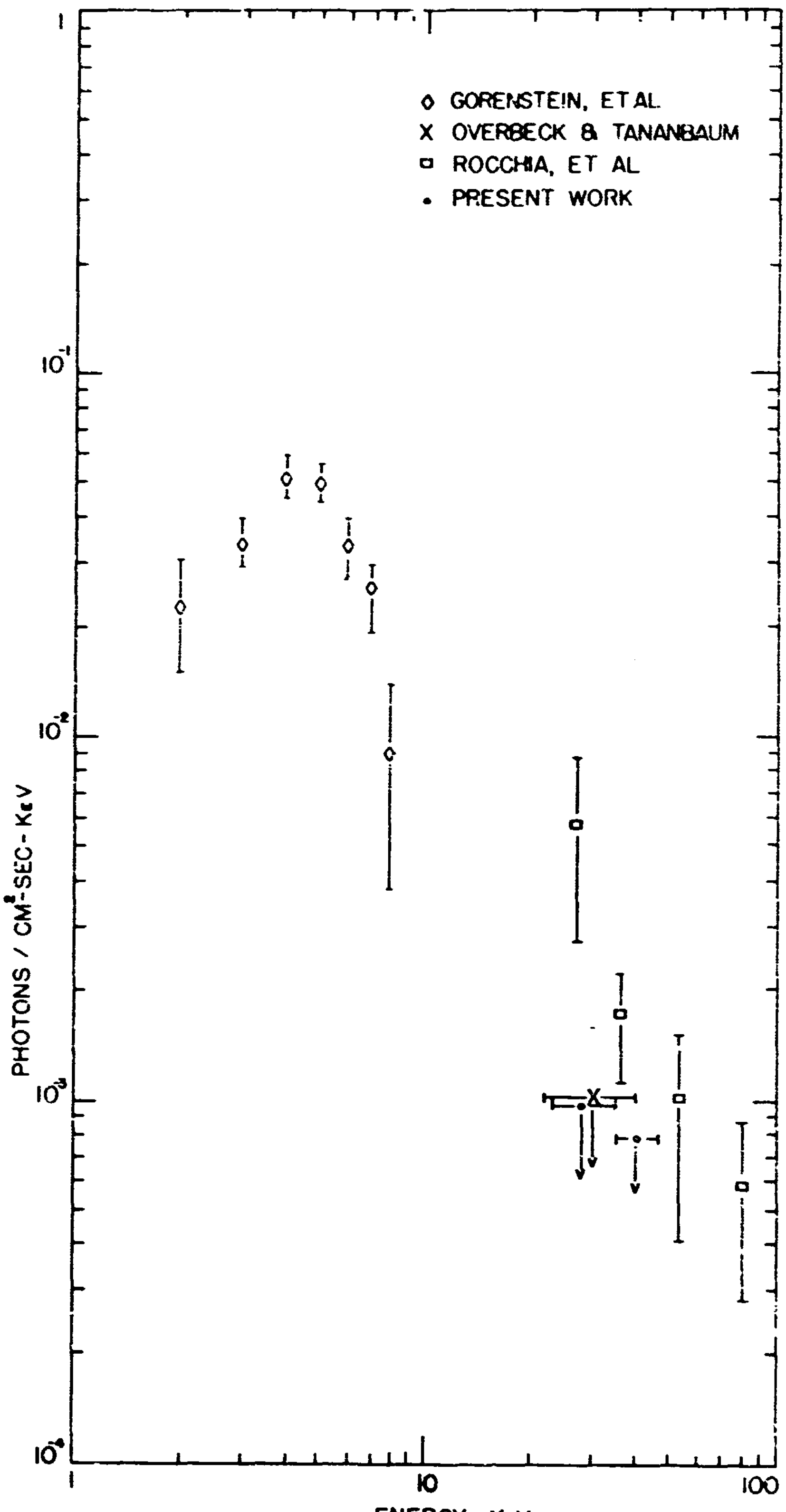
◇ GORENSTEIN, ET AL
X OVERBECK & TANANBAUM
▫ ROCCHIA, ET AL
• PRESENT WORK
PHOTONS / CM²-SEC-KeV
ENERGY, KeV
1
10^{-1}
10^{-2}
10^{-3}
10^{-4}
10
100

Figure 2⌊

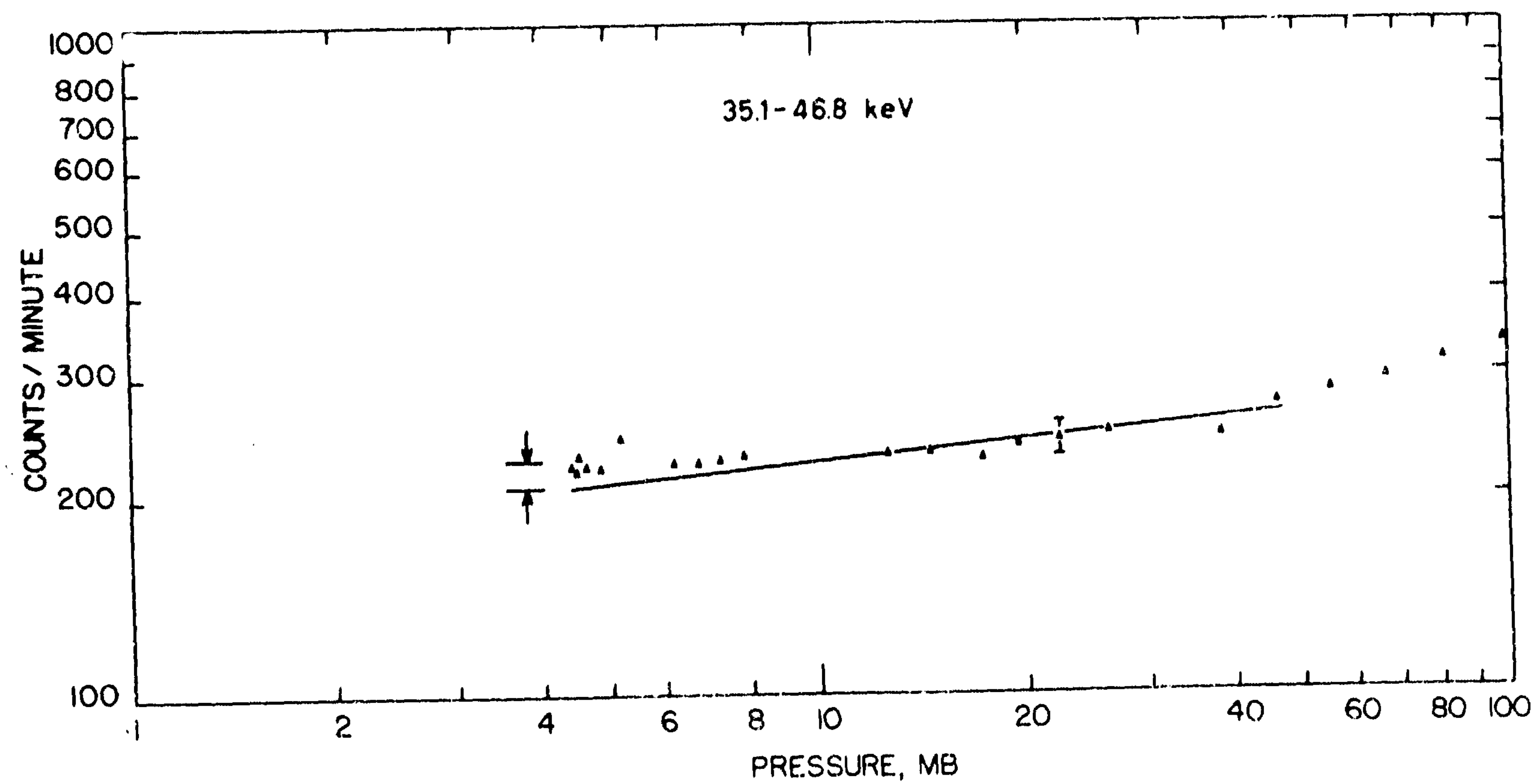
35.1-46.8 keV
COUNTS / MINUTE
1000
800
700
600
500
400
300
200
100
1
2
4
6
8
10
20
40
60
80
100
PRESSURE, MB

Figure 23

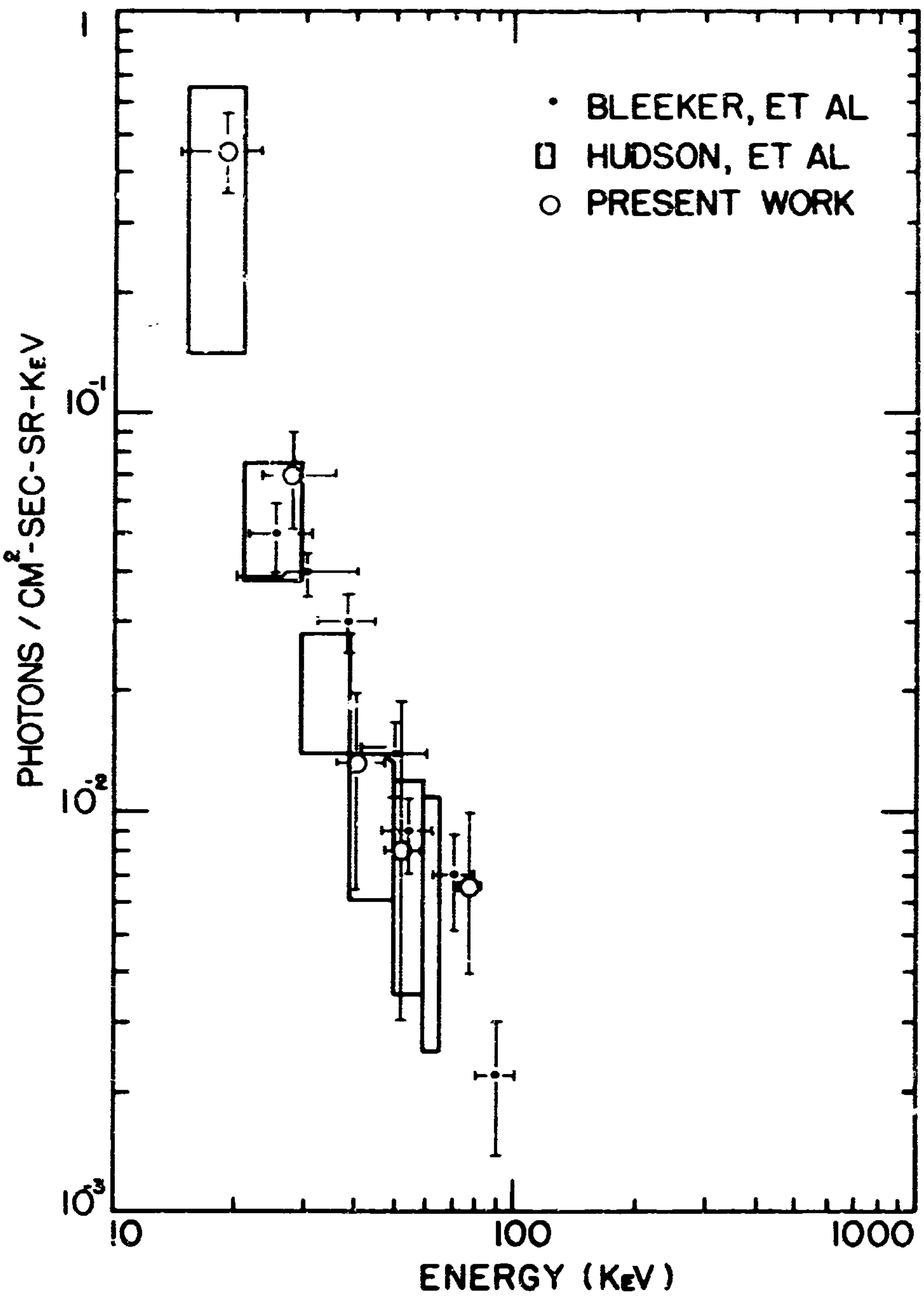

BLEEKER, ET AL
HUDSON, ET AL
PRESENT WORK
PHOTONS / CM^2-SEC-SR-KeV
1
10^{-1}
10^{-2}
10^{-3}
10
100
1000
ENERGY (KeV)

Figure 24

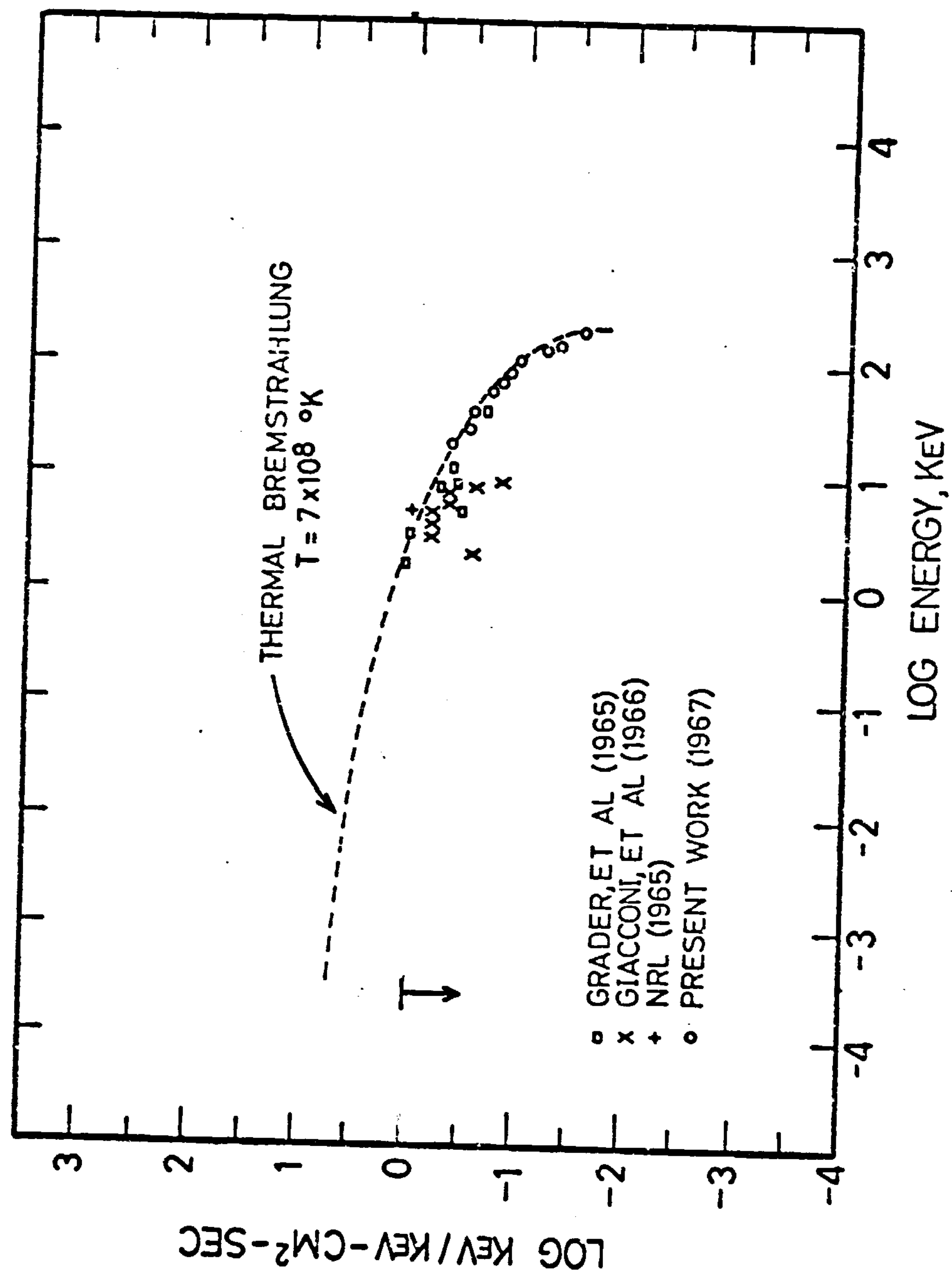
THERMAL BREMSTRAHLUNG
T = 7x108 °K
GRADER, ET AL (1965)
GIACCONI, ET AL (1966)
NRL (1965)
PRESENT WORK (1967)
LOG ENERGY, KeV
LOG KeV / KeV-CM2-SEC
-4
-3
-2
-1
0
1
2
3
4

FIGURE 25

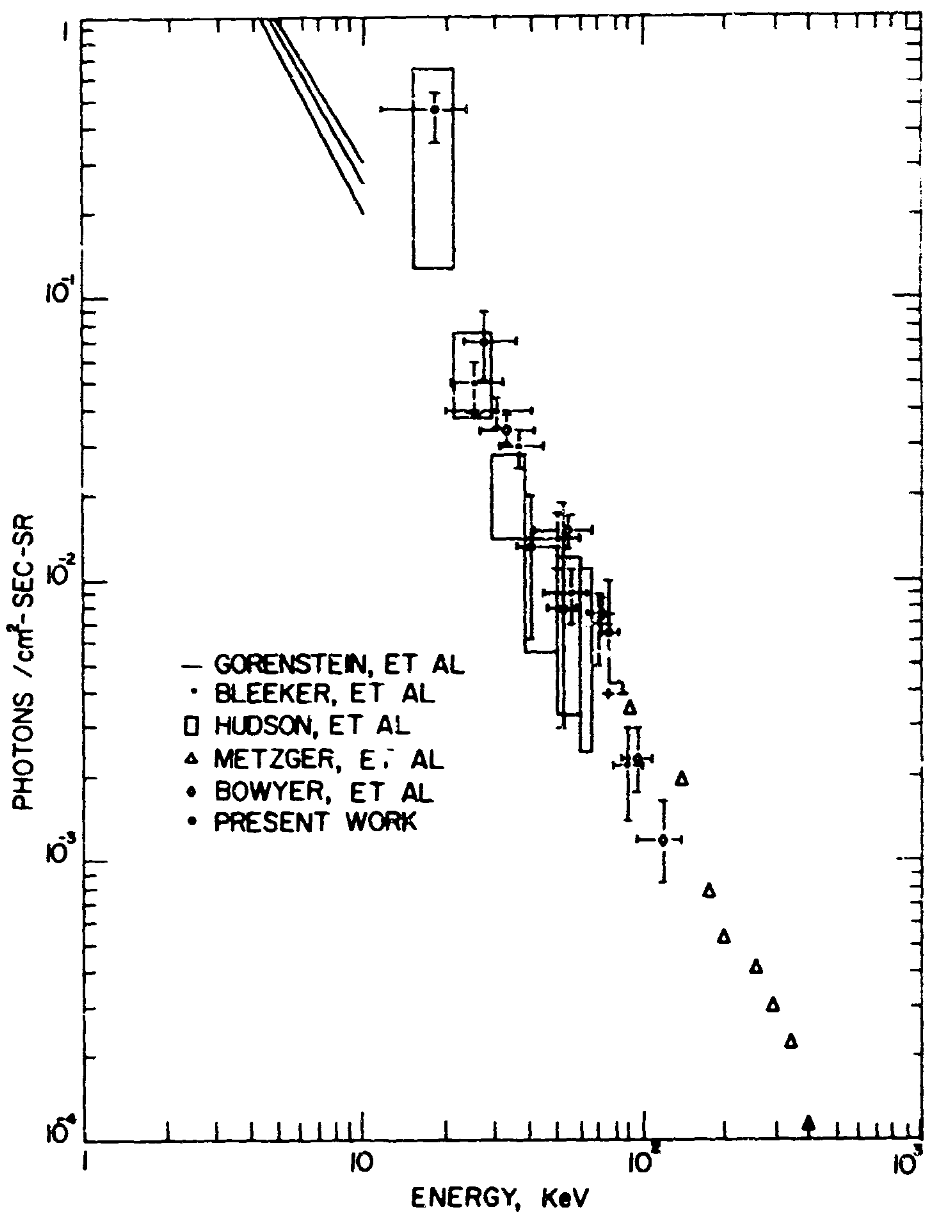

PHOTONS /cm²-SEC-SR
ENERGY, KeV
— GORENSTEIN, ET AL
· BLEEKER, ET AL
□ HUDSON, ET AL
△ METZGER, ET AL
◆ BOWYER, ET AL
• PRESENT WORK

Figure 26

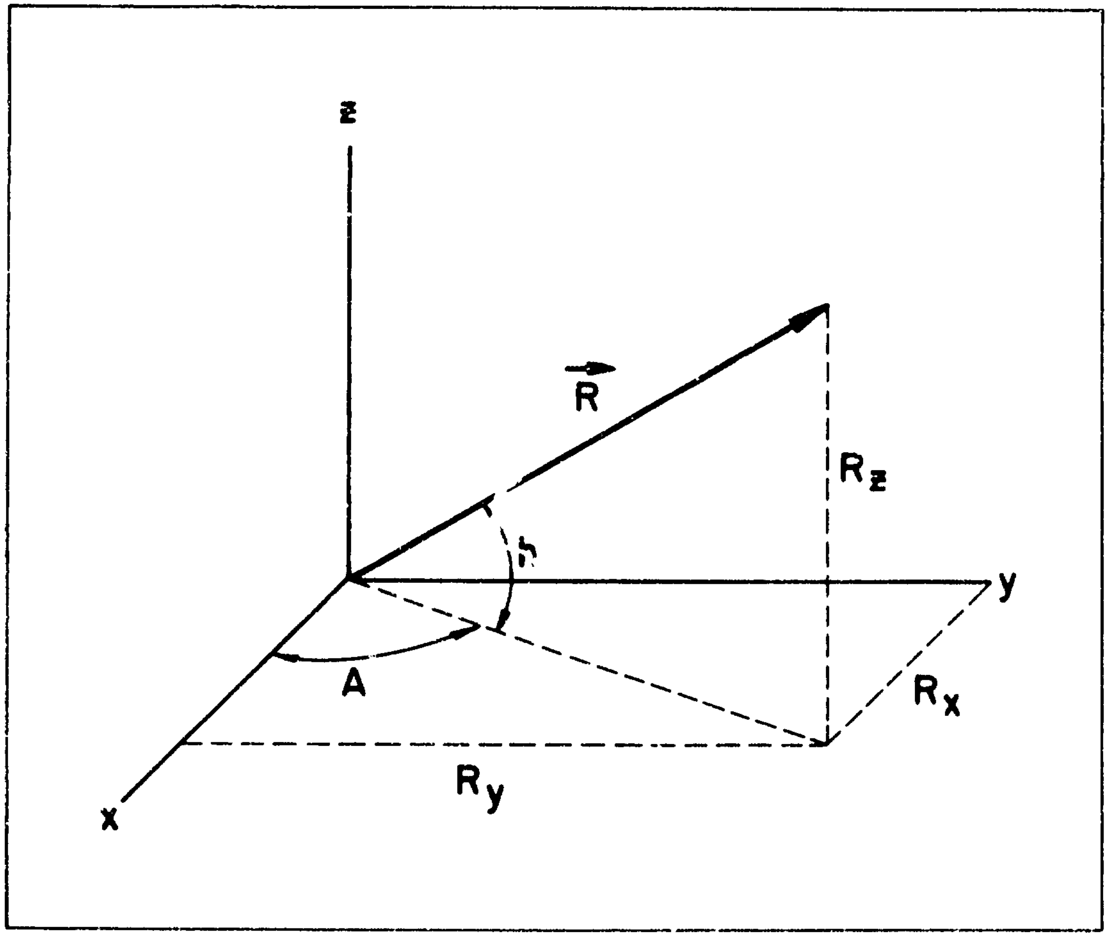

Figure 27

A BALLOON BORNE X-RAY SURVEY OF THE CYGNUS REGION

ERRATA

Page 38, line 12 should be:

$$\nu_M = \frac{3}{2} \left(\frac{E}{mc^2}\right)^2 \nu_c \stackrel{\sim}{=} \gamma^2 \nu_c .$$

Page 41, line 5 should be:

$$\ldots \nu \cong 3 \times 10^{13} \text{ c/sec} \ldots$$

and line 6 should be:

$$\ldots \nu \cong 2 \times 10^{19} \text{ c/sec} \ldots$$

Page 42, line 17 should be:

...If we try $B \sim 10^{-5}$ gauss,...

Page 52, line 9 should be:

...is conveniently available,[44]...

Page 53, line 4 should be:

...is the angle desired. $|\vec{R}_1|$, $|\vec{R}_2|$ are...

Page 54, line 9 should be:

$$R_T - R_T R_m \Delta T = R_m, \text{ or } R_T = \frac{R_m}{1 - T R_m} .$$

Page 62, line 6 should be:

Dvoracek,...